Mathematical modeling of bipolar resistive switching mechanism

By

Manasi Hemant Kulkarni

B.Tech. Visvesvaraya National Institute of Technology, Nagpur, India

THESIS

Submitted as partial fulfillment of the requirements for the degree of Master of Science in Materials Engineering in the Graduate College of the University of Illinois at Chicago, 2014

Defense Committee:

Prof. Eduard Karpov, Advisor

Prof. Didem Ozevin

Prof. Craig D. Foster

ACKNOWLEDGEMENTS

I would like to profusely thank my advisor, Dr. Eduard Karpov, for his constant encouragement and guidance. He has been a true inspiration for me and always motivated me to deliver my best in all academic endeavors. I greatly appreciate his insightful comments and invaluable advice.

I take this opportunity to extend my special thanks to all my committee members, Dr. Didem Ozevin and Dr. Craig Foster for their time and support.

Last but not the least, I would like to thank my parents and family who have always stood by me during tough times. I owe all my accomplishments to their never-ending love, support and prayers.

TABLE OF CONTENTS

TABLE OF CONTENTS (continued)

LIST OF FIGURES

LIST OF FIGURES (continued)

LIST OF TABLES

1. INTRODUCTION

Recently, transition metal oxide materials showing bipolar resistive switching have attracted deep interest. These materials have an application as resistive random access memory (RRAM) which shows advantages over capacitance based RAMs and even other resistance based RAMs [2] as well as memristor devices [8][9] and neuromorphic memories. Resistive switching is a phenomenon where the dielectric oxide material shows characteristic bi-stable resistance states, a high-resistance state and a low-resistance state, under the action of strong electric field or current [3].

Resistive switching can be classified in two types, unipolar resistive switching and bipolar resistive switching. Unipolar resistive switching is not dependent on applied voltage polarity and the set and reset switching can occur in same or opposite polarities. Whereas, bipolar resistive switching is dependent on polarity of applied voltage, i.e., if the set switching occurs under one polarity, reset switching occurs under another polarity [2].

In this thesis, an advanced mathematical model representing reactions taking place in the Pt/TiO_2/Pt resistive cell was created based on the mechanism for bipolar resistive switching explained in Jeong et al [1][13]. The model was then modified suiting to a set of experimental results and simulated to compare the results with experimental data.

The physical origin of the mechanism behind the bipolar resistive switching effect has been discussed and found to be based on formation and rupture of conduction paths. The mechanism of BRS can be classified into anion- and cation-migration-induced BRS

and electronic BRS. The anion-migration-induced mechanism includes the migration of anions, due to the drift-diffusion, and their electrochemical reactions at the interface between the anode and the switching material leads to changes in the resistance. The electronic BRS deals with the resistive switching resulting from the change in electronic transport behavior including the electronic charge injection at the cathode, and the trapping and de-trapping of electronic carriers [2].

2. LITERATURE REVIEW

Here, the background and motivation for the modeling of resistive switching mechanism is explained in greater detail.

Materials showing resistive switching behavior can include a spectrum of materials from magneto-resistance materials to phase change materials, but in the thesis, we are specifically considering the transition metal oxide materials. Transition metal oxide materials show two types of resistive switching, unipolar resistive switching and bipolar switching. The mechanism of unipolar resistive switching (URS) is assessed to be 'fuse-antifuse of conduction paths' [2]. Unipolar resistive switching has been observed in many binary transition metal oxides. The mechanism of bipolar resistive switching is considered to be the migration of anions. The anion-migration- based resistive switching has been most often observed in perovskite-type oxides so that 'anion' mainly denotes an oxygen ion [2]. TiO_2 shows both types of resistive switching, unipolar and bipolar, by altering the electroforming parameters and the applied voltage. In this thesis, we are considering to simulate the migration of anions mechanism leading to bipolar switching in $Pt/TiO_2/Pt$ cell. Thus, brief overview on bipolar resistive switching is presented in the further Section.

2.1. Bipolar resistive switching:

Some transition metal oxide (TMO) materials show hysteretic current-voltage (I-V) behavior denoting the switching between two characteristics resistance states, a high-resistance state (HRS) and a low-resistance state (LRS). This is a resistive

switching phenomenon which can be achieved by controlling applied voltage. The switching from the LRS to the HRS is termed reset switching and the switching the other way than the reset switching, i.e. from HRS to LHS, is termed set switching. If a voltage as high as one switching voltage is applied to a switching cell, the resistive switching takes place, that is, unless the applied voltage is as high as the switching voltage, no change in the resistance state takes place [2]. This resistive switching behavior is nonvolatile and thus can be applied to nonvolatile memory devices like RRAM.

The resistive switching behavior in the transition metal oxides can be classified into two categories, unipolar and bipolar resistive switching denoted by URS and BRS respectively. The URS behavior is not dependent on polarity, but only on amount of applied voltage. For example, if set switching takes place under one voltage polarity, then the reset switching can take place under both voltage polarities denoting that the polarity of switching voltage does not influence the following switching behavior. Therefore, an amount of the voltage applied to a switching cell is important for the URS operation rather than the applied voltage polarity [2]. However, in BRS an amount of voltage as well as the applied voltage polarity plays a very crucial role in the resistive switching. If the set switching takes place under one voltage polarity, the reset switching takes place under the other voltage polarity i.e. the set and the reset switching voltages are opposite to each other. Therefore, both an amount of the applied voltage and its polarity must satisfy proper conditions for the BRS operation unlike the URS.

2.2. Mechanism of Resistive Switching

The resistive switching mechanism has not been clarified yet, leaving many open questions. Nevertheless, local conduction paths in a switching material are estimated to be involved in the resistive switching [1]. Electroforming plays a significant role in the formation of the conduction paths. During the electroforming process a large amount of electric energy is provided for a switching cell so that the power dissipation in the cell reaches a certain threshold which causes to change the local microstructure of the cell, forming the conduction paths [2].

The mechanism of unipolar resistive switching (URS) is hypothesized to be 'fuse-antifuse of conduction paths'. Unipolar resistive switching has been observed in many binary transition metal oxides. Whereas, the mechanism of bipolar resistive switching is considered to be the migration of anions. The anion-migration-based resistive switching has been most often observed in perovskite-type oxides. The 'anion' mainly denotes an oxygen ion in these resistive switching cells. We will study anion migration induced resistive switching mechanism in detail because titanium dioxide shows anion migration induced mechanism of bipolar resistive switching.

2.2.1. Bipolar resistive switching Mechanism:

Perovskite-type ternary oxides which show bipolar resistive switching mechanism fall into this category. The BRS behavior in (Ba,Sr)TiO3, SrZrO3, SrTiO3, and (Pr,Ca)MnO3 has been frequently reported [2]. Recently, it has been reported that TiO_2 shows BRS behavior. The migration of the anions (oxygen ions) and their reactions at the interface between the anode and the switching material causes bipolar resistive

switching in these systems. The conduction paths are considered to be composed of oxygen-deficient non-stoichiometric phases with a conductivity higher than that of the stoichiometric phase [1].

At the anode of the switching cell, evolution of gas bubbles was observed during electroforming. This phenomenon possibly indicates the formation of oxygen gas at the interface. Also, the dependence of BRS on the polarity of the electroforming voltage showed that bipolar switching involves the migration of charged particles, oxygen ions/vacancies and electrons [1]. By these observations oxygen ion/vacancy migration and their reactions are judged to play a crucial role in the BRS behavior in the transition metal oxide switching cells thus categorizing it as anion migration induced switching. But the role of migration of charged particles needs more elaboration.

3. NUMERICAL PROCEDURE

3.1. Theoretical background

The BRS in $Pt/TiO_2/Pt$ is due to the oxygen-involved electrochemical reaction occurring at the Pt/TiO_{2-x} interfaces. The electrochemical reaction leads to the formation and annihilation of oxygen vacancies at the interfaces. The oxygen vacancy distribution changes with application of voltage, that is, the concentration in the vicinity of the cathode will be increased while that of anode will be decreased due to the drift of oxygen vacancies [1]. The electrochemical reaction whose reaction rate constant k can be given by a function of the applied voltage so that the flux of the oxygen ions/vacancies, taking part in the reaction, as a function of the applied voltage can be determined.

The oxygen vacancies in TiO_2 are donors, so that electroformed TiO_2 is regarded as heavily doped n type semiconductor. The TiO_{2-x} having oxygen vacancies as compared to stoichiometric TiO_2 apparently shows a higher ionic contribution to the electric current. The oxygen vacancies in TiO_2 increase the quantity of delocalized conduction electrons [16]. These oxygen vacancies in the non-stoichiometric layer are ionized and function as mobile space charges [7]. The SBH at a metal/insulator is influenced by the space charge density and its distribution in the insulator, where SBH at the interface between a metal and n-type semiconductor decreases as increasing the positive space charge density [1]. The calculation of oxygen vacancy distribution should be determined in a time domain at various because the quasistatic approximation is not practical due to their low diffusivity and also applied voltage plays an important factor in the variation of oxygen vacancies. It can be hypothesized depending on Poisson equation that, a change in the voltage distribution in TiO_{2-x} indicating a change in the profile of the conduction

and the valance bands is due to the time dependent oxygen vacancies variation under a certain voltage. And the change might be responsible to the time dependent change in resistance based on the variation of electron transport behavior. Thus, the time dependent distribution of oxygen vacancies and electrons needs to be studied to look into the time dependent bipolar switching behavior [1].

The distribution of the oxygen vacancies in TiO_{2-x} and its variation with respect to time can be obtained by solving the time-dependent one-dimensional drift- diffusion equation of the oxygen vacancies and the electrons using the finite difference method, considering the Pt/TiO_{2-x}/Pt junction as a one-dimensional system. As a solution of the drift-diffusion equations, the *I-V* curve of the Pt/ TiO_{2-x} /Pt junction can be obtained.

3.2. Formation of model

In this thesis, the calculation is accomplished by considering a simplified one dimensional Pt/TiO_{2-x}/Pt junction. The mechanism of the BRS is considered in terms of redox reactions involving oxygen ions and oxygen vacancies at the Pt/TiO_2 interfaces. The Wolfram alpha software Mathematica 9 was used to solve the time-dependent one-dimensional drift- diffusion equation of the oxygen vacancies using the finite difference method [12]. Also, Fick's second law was used to calculate the distribution of oxygen ions due to applied voltage.

The principle of finite difference methods is to solve ordinary differential equations. The derivatives are replaced in the equation using difference quotients to approximate the differential operator in this method. These approximations are simulated at space and time points by dividing the domain in space and in time [6]. The truncation

error or discretization error is the error caused by going from the exact solution based the differential operator to the numerical solution based on the difference operator. The error in finite difference method's solution is defined as the difference between its approximation and the exact analytical solution [10].

We will consider the one-dimensional case to formulate the equation. The main theory behind any finite difference scheme is related to the definition of the derivative of a smooth function *u* at a point *x*:

$$u'(x) = \lim_{h \to 0} \frac{u(x+h) - u(x)}{h},$$

and to the fact that when *h* tends to zero, the equation on the right-hand side provides a good approximation of the derivative [10]. That means, *h* should be sufficiently small to get a good approximation. The finite difference quotient is used to solve the drift diffusion differential equation by Euler method [4]. Thus, the Pt electrodes and TiO_{2-x} layer were discretized [14].

Figure 3.1 shown below is the configuration of a $Pt/TiO_2/Pt$ switching cell. The electrochemical reaction will be dealt with at the two interfaces between the left electrode (LE) and TiO_{2-x} and between TiO_{2-x} and the right electrode (RE), where a Helmholtz layer is formed at the metal – semiconductor interfaces. This Helmholtz layer is due to the separation of two oppositely charged layers, one on the metal side while other on the semiconductor side at the interface. The oxygen ions in metal are negatively charged rather than neutral so that they can participate in the electrochemical reaction of the formation and annihilation of oxygen vacancies dependent on applied voltage taking place at the interface [1].

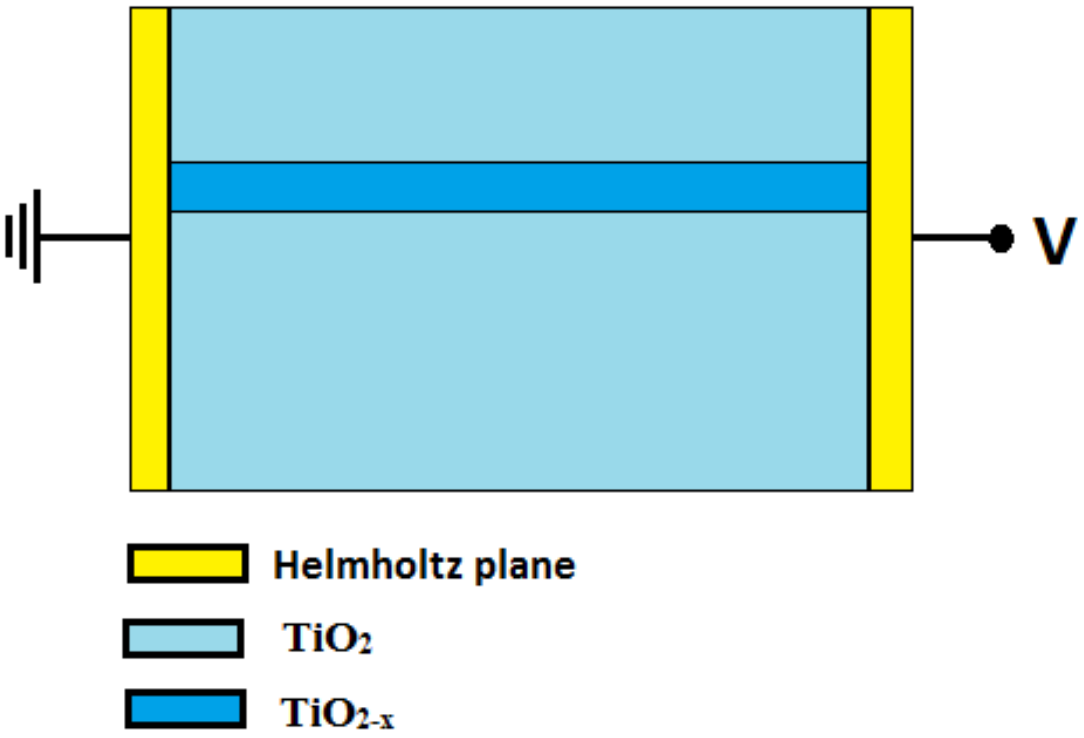

Figure 3.1. Configuration of a Pt/TiO_2/Pt switching cell

The configuration of nodes in TiO_{2-x} layer as shown in Figure 3.2. Similar approach of discretizing into nodes is used for the electrodes. Along the spatial coordinate *x*, *NL* nodes are assigned to the Pt left electrode (LE), *N* nodes to TiO_{2-x}, and also *NR* nodes to the Pt right electrode (RE). The thicknesses of the LE, TiO_{2-x}, and RE are considered to be *dL*, *d* and *dR*, respectively. Hence, the distance between neighboring nodes in the left electrode can be expressed as $dL = (NL - 1)$ while that in the right electrode as $dR = (NR - 1)$ while that in TiO_{2-x} *is* $d = (N - 1)$.

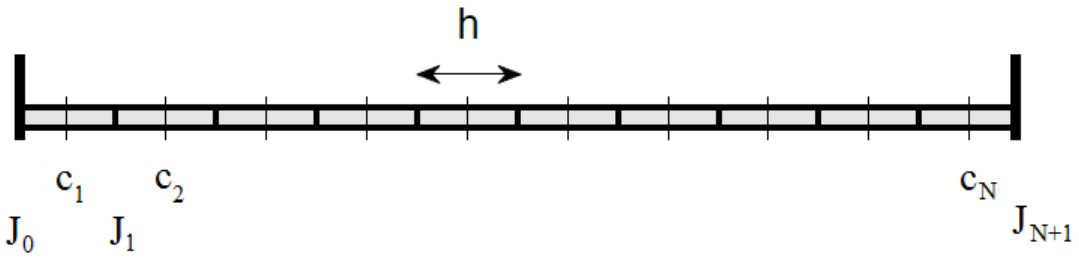

Figure 3.2. Nodes of Pt/TiO_2/Pt switching cell

The one dimensional time dependent distribution of oxygen ions, oxygen vacancies and electrons in the Pt electrode and TiO_2 dielectric layer respectively can be calculated using drift - diffusion equation given by,

$$J^{i}_{DD} = z_i \mu_i c_i E - D_i\left(\frac{\partial c}{\partial x}\right) \quad (1)$$

Table 3.1. Acronyms used in equation (1)

Symbol	Description
J_{DD}	Drift diffusion flux
z	Charge number
μ	Mobility
c	Concentration of particle
E	Electric field
D	Diffusivity of particle
i	Particle (ion, vacancy, electron)

Differentiation with respect to 't', Fick's second law is expressed as

$$\frac{\partial c_i(x,t)}{\partial t} = -\partial J^{i}_{DD}/\partial x \quad (2)$$

$$\frac{\partial c_i(x,t)}{\partial t} = -z_i\mu_i c_i(x)\frac{\partial E}{\partial x} - z_i\mu_i E(x)\frac{\partial c_i}{\partial x} + D_i\frac{\partial^2 c_i}{\partial x^2} \quad (3)$$

Thus, the equation (2) can be discretized as follows,

$$\frac{c_i(x,t+\Delta t)-c_i(x,t)}{\Delta t} = \frac{1}{\Delta x}\left(j_{t,x-\Delta x/2} - j_{t,x+\Delta x/2}\right) \quad (4)$$

First we will formulate the distribution of oxygen ions in both the electrodes. Oxygen ions get chemisorbed at the grain boundaries because of the electrochemical reaction taking place at the interface of Pt/TiO_2.

The oxygen flux in the electrodes is only due to diffusion while the drift of oxygen ions in the electrode can be ignored because electric field is absent in the metal.

Thus the flux of oxygen ions at the nodes can be given as follows

$$j_{t,x+1/2} = \frac{NL-1}{d} D\left(c_{t,x+1} - c_{t,x}\right) \quad (5)$$

$$j_{t,x-1/2} = -\frac{NL-1}{d} D\left(c_{t,x} - c_{t,x-1}\right) \quad (6)$$

Thus, to calculate the time dependent diffusion of oxygen ions, Equation (5) and Equation (6) and entered into Equation (4), and can be expressed in matrix form [11] as

$$\frac{\partial c_i(x,t)}{\partial t} = \frac{D_i(NL-1)^2}{dL^2}\begin{bmatrix} -2 & 1 & 0 & \dots & \dots & 0 \\ 1 & -2 & 1 & \dots & \dots & 0 \\ 0 & 1 & -2 & 1 & \dots & 0 \\ \vdots & & \ddots & & : & \vdots \\ & & & & & : \\ \dots & 0 & 0 & 0 & 1 & -2 \end{bmatrix}\begin{matrix} c1 \\ c2 \\ c3 \\ : \\ : \\ cn \end{matrix}$$

$$\frac{\partial c_i(x,t+1)-\partial c_i(x,t)}{\partial t} = \frac{D_i(NL-1)^2}{dL^2}\begin{bmatrix} -2 & 1 & 0 & \dots & \dots & 0 \\ 1 & -2 & 1 & \dots & \dots & 0 \\ 0 & 1 & -2 & 1 & \dots & 0 \\ \vdots & & \ddots & & : & \vdots \\ & & & & & : \\ \dots & 0 & 0 & 0 & 1 & -2 \end{bmatrix}\begin{matrix} c1 \\ c2 \\ c3 \\ : \\ : \\ cn \end{matrix} \quad (7)$$

To approximate the values of concentration of oxygen ions at each time step the equation (7) can be solve by Euler's method.

Similarly, the drift diffusion equation is used to calculate the time dependent drift diffusion of oxygen vacancies in the TiO_{2-x}. As, both the drift and diffusion of the oxygen vacancies and the electrons must be taken into account during calculation of the oxygen vacancy and the electron distributions in oxygen deficient layer makes the calculation more complicated.

Thus, drift diffusion equation of both particles, (electron and oxygen vacancies) at each node can be expressed by discretization of equation (1),

$$j_{t,\,x+1/2} = -\frac{1}{2d} z_i \mu_i \,(c_{t,n+1} + c_{t,n})\,(N-1)\,(V_{t,n+1} - V_{t,n}) - \frac{N-1}{d} D\,(c_{t,n+1} - c_{t,n}) \quad (8)$$

$$j_{t,\,x-1/2} = -\frac{1}{2d} z_i \mu_i \,(c_{t,n} + c_{t,n-1})\,(N-1)\,(V_{t,n} - V_{t,n-1}) - \frac{N-1}{d} D\,(c_{t,n} - c_{t,n-1}) \quad (9)$$

Thus, Fick's second law in matrix form [11] can be

$$\frac{\partial c_i(x,t)}{\partial t} =$$

$$\frac{z_i \mu_i (N-1)^2}{2d^2} \begin{bmatrix} +V0 - 2V1 + V2 & V2 - V1 & 0 & \dots & \dots & 0 \\ V1 - V2 & +V1 - 2V2 + V3 & V3 - V2 & \dots & \dots & 0 \\ 0 & V2 - V3 & +V2 - 2V3 + V4 & V2 - V3 & \dots & 0 \\ \vdots & & V(n-1) - V(n) & +V(n-1) - 2Vn + V(n+1) & V(n+1) - V(n) & \vdots \\ & & & & 0 & : \\ \dots & 0 & 0 & 0 & V(N-1) - V(N) & +V(N-1) - 2VN + V(N+1) \end{bmatrix} \begin{matrix} c1 \\ c2 \\ c3 \\ cn \\ : \\ cN \end{matrix}$$

$$+ \frac{D_i (N-1)^2}{d^2} \begin{bmatrix} -2 & 1 & 0 & \dots & \dots & 0 \\ 1 & -2 & 1 & \dots & \dots & 0 \\ 0 & 1 & -2 & 1 & \dots & 0 \\ \vdots & & \ddots & & : & \vdots \\ & & & & & : \\ \dots & 0 & 0 & 0 & 1 & -2 \end{bmatrix} \begin{matrix} c1 \\ c2 \\ c3 \\ : \\ : \\ cn \end{matrix}$$

Table 3.2 Acronyms used in equation (10)

Symbol	Description
d	Thickness of the layer
N	Total number of nodes in the layer
$\Delta x = d/(N- 1)$	distance between two consecutive nodes

Assuming that, V varies linearly from $V(0) = 0$ to $V(d) = V$,

$V1 - V2 = V2 - V3 = -1\ V$

$+V0 - 2V1 + V2 = +V1 - 2V2 + V3 = 0\ V$

$V2 - V1 = V2 - V1 = 1\ V$

Therefore the above equations can be written as,

$$\frac{\partial c_i(x,t)}{\partial t} = \frac{z_i \mu_i (N-1)^2}{2d^2} V \begin{bmatrix} 0 & 1 & 0 & \dots & \dots & 0 \\ -1 & 0 & 1 & \dots & \dots & 0 \\ 0 & -1 & 0 & 1 & \dots & 0 \\ \vdots & & \ddots & 0 & : & \vdots \\ & & & & 0 & : \\ \dots & 0 & 0 & 0 & -1 & 0 \end{bmatrix} \begin{matrix} c1 \\ c2 \\ c3 \\ : \\ : \\ cn \end{matrix} + \frac{Di(N-1)^2}{d^2} \begin{bmatrix} 2 & -1 & 0 & \dots & \dots & 0 \\ -1 & 2 & -1 & \dots & \dots & 0 \\ 0 & -1 & 2 & -1 & \dots & 0 \\ \vdots & & \ddots & & : & \vdots \\ & & & & & : \\ \dots & 0 & 0 & 0 & -1 & 2 \end{bmatrix} \begin{matrix} c1 \\ c2 \\ c3 \\ : \\ : \\ cn \end{matrix} \quad (10)$$

$= \mathbf{A}*c + \mathbf{B}*c$

Where, $\mathbf{A} = \frac{z_i \mu_i (N-1)^2}{2d^2} V \begin{bmatrix} 0 & 1 & 0 & \dots & \dots & 0 \\ -1 & 0 & 1 & \dots & \dots & 0 \\ 0 & -1 & 0 & 1 & \dots & 0 \\ \vdots & & \ddots & 0 & : & \vdots \\ & & & & 0 & : \\ \dots & 0 & 0 & 0 & -1 & 0 \end{bmatrix}$

$$\mathbf{B} = \frac{Di(N2-1)2}{(d2)2}\begin{bmatrix} 2 & -1 & 0 & \dots & \dots & 0 \\ -1 & 2 & -1 & \dots & \dots & 0 \\ 0 & -1 & 2 & -1 & \dots & 0 \\ \vdots & & \ddots & & : & \vdots \\ & & & & & : \\ \dots & 0 & 0 & 0 & -1 & 2 \end{bmatrix}$$

And c is the concentration vector, n is number of nodes, m is m^{th} time step as $c_m = c\ (t = t_m)$

The Euler method is one of the most basic numerical procedure in mathematics and computational science for solving ordinary differential equations (ODEs) with an initial value [17]. It is the simplest Runge Kutta method for numerical integration of ordinary differential equations [17]. Euler's rule is used to predict the approximate value of the next time step which is dependent on the input of initial value. Here the requirement of solving the model needs the approximate next step values after regular time interval. Thus, Euler's rule was used to solve this mathematical model. Euler's rule is defined as follows [17],

To approximate the solution for initial value problem,

$$y'\ (t) = f\ (t, y\ (t))\ , \qquad y\ (t_o) = y_o$$

Consider a value Δt for every time step size and then set " $t_n = t_0 + n\Delta t$ ",

Now, the next step of the Euler method from t_n to $t_{n+1} = t_n + \Delta t$ is

$$y_{n+1} = y_n + \Delta t * f\ (t_n, y_n\ ).$$

Similarly, to approximate the values of concentration at each time step i.e. to solve the equation (10) by substituting in equation (4), it can be expressed using explicit forward Euler's method [6] as

$c_{m+1} = c_m + \Delta t\ (\mathbf{A} + \mathbf{B}) * c_m$

Where, c is the concentration vector of oxygen vacancies at all nodes.

To solve this equation, we require boundary conditions and initial concentration profile of oxygen vacancies. The boundary condition is assumed that zero flux is flowing from each of the electrodes into the electrolyte. The influence of applied voltage on the drift of oxygen vacancies was taken into consideration. And various different initial concentration profiles of oxygen vacancies were assumed.

Once the concentration profiles at all nodes for every time step was calculated, then the flux at the midpoints of the cell was to be calculated [5]. Flux is defined as the flow of a physical property in space and here the flux i.e. the current density of oxygen vacancies was calculated.

As shown in the Figure 3.2, the flux was calculated at the center of two nodes by the following equation,

$$j_{t,\,x\text{-}1/2} = -\frac{1}{2d} z_i \mu_i \left(c_{t,n} + c_{t,n\text{-}1}\right)(N-1)\left(V_{t,n} - V_{t,n\text{-}1}\right) - \frac{N-1}{d} D\left(c_{t,n} - c_{t,n\text{-}1}\right) \qquad (11)$$

This equation is the discretized version [14] of the drift diffusion equation, and it is based on the concentration of oxygen vacancies at every time step and the applied voltage.

To calculate the flux, the equation (11) can be written in matrix form as

$$\frac{\partial c_i(x,t)}{\partial t} = \frac{z_i \mu_i (N-1)}{2d} \begin{bmatrix} V1-V0 & 0 & 0 & \dots & \dots & 0 \\ V2-V1 & V2-V1 & 0 & \dots & \dots & 0 \\ 0 & V3-V2 & V3-V2 & 0 & \dots & 0 \\ \vdots & & V(n)-V(n-1) & V(n)-V(n-1) & 0 & \vdots \\ & & & & \dots & \vdots \\ \dots & 0 & 0 & 0 & & V(N)-V(N-1) \end{bmatrix} \begin{matrix} c1 \\ c2 \\ c3 \\ cn \\ \vdots \\ cN \end{matrix}$$

$$+ \frac{D_i (N-1)}{d} \begin{bmatrix} 0 & 0 & 0 & \dots & \dots & 0 \\ -1 & 1 & 0 & \dots & \dots & 0 \\ 0 & -1 & 1 & 0 & \dots & 0 \\ \vdots & & \ddots & & \vdots & \vdots \\ & & & & -1 & 1 \\ \dots & 0 & 0 & 0 & 0 & 0 \end{bmatrix} \begin{matrix} c1 \\ c2 \\ c3 \\ \vdots \\ \vdots \\ cn \end{matrix} \qquad (12)$$

As, V in the system is assumed to vary linearly from $V(0) = 0$ to $V(d) = V$,

The elements in the matrix in equation (12) can be interpreted as

$V2 - V1 = V3 - V2 = 1\ V$

Therefore the above equations can be written as,

$$J_t = \frac{z_i \mu_i (N-1)}{2d} V \begin{bmatrix} 1 & 0 & 0 & \dots & \dots & 0 \\ 1 & 1 & 0 & \dots & \dots & 0 \\ 0 & 1 & 1 & 0 & \dots & 0 \\ \vdots & & \ddots & & : & \vdots \\ & & & & 1 & 1 \\ \dots & 0 & 0 & 0 & 0 & 2 \end{bmatrix} \begin{matrix} c1 \\ c2 \\ c3 \\ : \\ : \\ cn \end{matrix} + \frac{\mathrm{D_i}(N-1)}{d} \begin{bmatrix} 1 & 0 & 0 & \dots & \dots & 0 \\ -1 & 1 & 0 & \dots & \dots & 0 \\ 0 & -1 & 1 & 0 & \dots & 0 \\ \vdots & & \ddots & & : & \vdots \\ & & & & -1 & 1 \\ \dots & 0 & 0 & 0 & 0 & 1 \end{bmatrix} \begin{matrix} c1 \\ c2 \\ c3 \\ : \\ : \\ cn \end{matrix} \quad (11)$$

$$= \mathbf{P} + \mathbf{Q}$$

Where, $\mathbf{P} = \frac{z_i \mu_i (N-1)}{2d} V \begin{bmatrix} 1 & 0 & 0 & \dots & \dots & 0 \\ -1 & 1 & 0 & \dots & \dots & 0 \\ 0 & -1 & 1 & 0 & \dots & 0 \\ \vdots & & \ddots & & : & \vdots \\ & & & & -1 & 1 \\ \dots & 0 & 0 & 0 & 0 & 1 \end{bmatrix}$

$$\mathbf{Q} = \frac{\mathrm{D_i}(N-1)}{d} \begin{bmatrix} 1 & 0 & 0 & \dots & \dots & 0 \\ -1 & 1 & 0 & \dots & \dots & 0 \\ 0 & -1 & 1 & 0 & \dots & 0 \\ \vdots & & \ddots & & : & \vdots \\ & & & & -1 & 1 \\ \dots & 0 & 0 & 0 & 0 & 1 \end{bmatrix}$$

These matrices were then modified depending on the boundary conditions and multiplied with the concentration profile vector at each time step to calculate the flux at the midpoint of every cell.

Mathematica is a very powerful computational software program used in many scientific, engineering, mathematical and computing fields, based on symbolic mathematics [15]. This software was used to write the code for the model . The Wolfram Language is the programming language used in Mathematica [15]. This software offers a broad range of advantages over the other similar software programs. Mathematica focuses on quality symbolic computation and features like unlimited precision arithmetic.

Various different codes were written to calculate the distribution of oxygen ions, oxygen vacancies and the flux variation of oxygen vacancies dependent on variation of voltage.

The platinum electrodes were considered to have homogeneous distribution of nodes along their width. A total of 10 nodes were assumed in each of the platinum electrodes. The boundary conditions were the flux of oxygen ions flowing from the TiO_{2-x} to the electrodes, thus the flux one end of the electrode was always kept zero while the flux at the node at the interface of electrode and the electrolyte was changed. A number of different boundary conditions were tried. The graphs of the variation of oxygen ions for each of the cases is plotted in Section (4).

The code in Appendix 1.1 represents a typical case to determine the distribution of oxygen ions in the left electrode while that in 1.2 represents a typical case to determine the distribution of oxygen ions in the right electrode and the similar codes can be used for all the cases with changing the variables and boundary condition. In the code, *V* is the applied voltage cycle and *Vp* is used to denote the plot of applied voltage. **B** is the matrix which is shown in the equation (7). It is altered to include the boundary conditions and **G** is the vector used to represent the boundary conditions. Having all the parameters needed

to approximate the concentration of oxygen ions at all nodes for next time steps, Euler's rule was used. The time step (Δt) for calculation of concentration of oxygen ions was 0.002. But the concentration profile was plotted at only few time intervals as the profile was varying infinitesimally at every time step.

Then, the focus was shifted to calculate variation of oxygen vacancies in the TiO_{2-x} layer. An initial density profile and proper boundary conditions were required to calculate the time dependent distribution of oxygen vacancies.

The initial density profile of oxygen vacancies after the initial electroforming procedure was studied from the paper (Jeong et. al) [1] and coded. The thickness of TiO_2 was set to 50 nm. The total number of nodes in the TiO_{2-x} layer were 272. These nodes were distributed unevenly, 36 nodes were assigned to each near interface regions and 200 nodes to the bulk because the changes in electron and oxygen vacancy densities as well as the internal voltage in the near metal- semiconductor interface regions were drastic as compared to the bulk of the film.

The code in Appendix 2.1 results in the initial density profile of oxygen vacancies after electroforming is completed. 'nodes1' and 'nodes3' are the 36 nodes each on left near interface and right near interface region respectively, while the 'nodes2' are the 200 nodes in the bulk. Similarly, 'den1', 'den2' and 'den3' represent the initial densities of the oxygen vacancies at each node. Tables named 'denp1', 'denp2', and 'denp3' were included to create density profile plot.

This initial concentration of oxygen vacancies was used to calculate the time dependent concentration variation of oxygen vacancies at every node. The code in

Appendix 3.1 represents a typical case and the similar code can be used for all the cases by changing the variables. The code was also used to calculate the time dependent flux variation at every node, the time dependent flux at the left most node i.e. the near interface node, and the flux variation with respect to the voltage. Variables used in the code are mentioned in the Table 3.3.

Table 3.3: Variables for the code in Appendix 3.1

Symbol	Description
m	Number of nodes
d_0	thickness of TiO_2 layer in cm
$D0_0$	diffusivity of particle in the code
x	number of node from the left interface for which the flux vs time and flux vs voltage graphs are plotted
M	maximum number of time steps
q	electron charge
f	Frequency of applied voltage

The TiO_{2-x} layer was discretized [14] as shown in the Figure 3.2, where the one dimensional space was discretized in *N* number of grid cells. The edges of the cells were the nodes used to calculate the concentration of oxygen vacancies and the center of the cells were the nodes used to calculate the current density of the oxygen vacancies.

In the code shown in appendix 3.1, the notations *a*, *b*, *a1*, *b1* are defined as the coefficients of the matrices **A** and **B** for calculating the concentration of oxygen vacancies at all nodes and coefficients of the matrices **P** and **Q** for calculating their flux at all nodes respectively. An alternating voltage was assumed to be applied to the system having amplitude of 1.6 V and frequency of 1 Hz. Matrices **A** and **B** represent the

matrices in equation (10) and are dependent on applied voltage, coefficients *a* and *b*. The addition of matrices **A** and **B** is defined as **K**. It is used in the calculation of concentration of oxygen vacancies by Euler's rule.

$C_{(0)}$ is defined as the initial profile of oxygen vacancies at all nodes. This initial profile is shown in the Figure 4.2.1. The density of oxygen vacancies near interface region is varying from 10^{20} to 10^{21} cm^3. This profile is directly taken from the code in Appendix 2.1. Having all the parameters needed to approximate the concentration of oxygen vacancies at all nodes for next time steps, Euler's rule was used. The time step for calculation of concentration of oxygen vacancies was 0.002. But the concentration profile was plotted at only few time intervals as the profile was varying infinitesimally at every time step.

To calculate the current density i.e. the flux of oxygen vacancies which was dependent on the concentration gradient, different set of variables were used. **P** is the matrix which represents the behavior dependent on the drift current while **Q** is the matrix which represents the behavior dependent on the diffusion current. **P** and **Q** represent the matrices shown and are dependent on applied voltage having coefficients *a1* and *b1* respectively. The addition of matrices **P** and **Q** is defined as **R**. The matrix **R** is used in the calculation of flux of oxygen vacancies at all nodes. The flux of the vacancies at all nodes at every time step was defined by the *J* and *Jp* is the flux profile of oxygen vacancies at few intervals.

Then the flux at a node '*x*' was plotted vs time at every time step. For the same node '*x*' the graph of current density vs voltage was plotted. The graphs resulting from this code are presented in the Section 4.2.

Table 3.4. Experimental data

Time (s)	mV	A
20518.8	1.776	2.00E-08
20604.61	319.857	1.90E-07
20694.61	640.138	4.90E-07
20793.61	959.759	8.90E-07
20914.2	1280.01	2.52E-06
21142.8	1600.137	3.46E-05
21480.6	1280.525	1.80E-05
20793.61	959.759	8.90E-07
21700.8	639.916	7.00E-08
21790.8	319.814	-7.80E-07
21877.2	-0.621	-7.80E-07
21963	-319.179	-5.70E-07
22053	-639.04	-4.70E-07
22152.6	-960.421	-4.50E-07
22273.21	-1280.363	-4.30E-07
22498.8	-1600.082	-4.50E-07
22839.6	-1280.253	-3.40E-07
22960.21	-960.291	-2.40E-07
23059.22	-640.899	-1.70E-07
23149.21	-321.083	-1.00E-07

3.3. Experimental details:

The experimental data achieved for a bipolar resistive switching cell is shown in Table 3.4. The graphs based on the experimental data are shown in Section 4.3. As we can see from the experimental data, the time period of the applied voltage cycle was large.

Based on the above model based anion migration induced mechanism for bipolar resistive switching, a similar model was assumed to formulate experimental data points but with certain changes. Thus, the model was simplified to be simulated for low frequencies of applied voltage and understand the behavior with clarity. Therefore, in this model, the initial concentration of oxygen vacancies was assumed to be symmetrical and fewer number of nodes were assumed as compared to the previous model based on the paper (Jeong et. al.) [1].

3.4. Model of experimental data

In the previous model, the thickness of TiO_2 electrolyte was assumed to be 50 nm while in this model it was set to 25 nm. The TiO_{2-x} layer was assumed to have 101 nodes. These nodes were distributed evenly along the length of the TiO_{2-x} layer. But the distribution of oxygen vacancies were distributed unevenly in the initial profile, higher densities at the near interface region and constant density of 10^{20} and 10^{21} cm^{-1} in the bulk.

The code in Appendix 2.2 results in the initial density profile of oxygen vacancies after electroforming is completed. 11 nodes each were considered in left near interface and right near interface region respectively, while 79 nodes were assumed in the bulk totaling the nodes to 101. ‘den1’, ‘den2’ and ‘den3’ represent the initial densities of the oxygen vacancies at each node. Tables named ‘denp1’, ‘denp2’, and ‘denp3’ were included to create density profile plot.

This initial concentration of oxygen vacancies was used to calculate the time dependent concentration variation of oxygen vacancies at every node. The code in Appendix 3.2 represents a typical case and the similar code can be used for all the cases with changing the variables. The code was also used to calculate the time dependent flux variation at every node, the time dependent flux at the left most node i.e. the near interface node, and the flux variation with respect to the voltage. Variables used in the code are mentioned in the Table 3.5.

Table 3.5 Acronyms for Appendix 3.2

Symbol	Description
m	Number of nodes
d_0	thickness of TiO_2 layer in cm
$D0_0$	diffusivity of particle in the code
x	number of node from the left interface for which the flux vs time and flux vs voltage graphs are plotted
M	maximum number of time steps
q	electron charge
f	Frequency of applied voltage
z	Charge number

In the code shown in Appendix 3.2, the variables *a*, *b*, *a1*, *b1* are defined as the coefficients of the matrices **A**, **B**, **P** and **Q** for calculating the concentration of oxygen vacancies at all nodes and their flux at all nodes respectively. An alternating voltage was assumed to be applied to the system having amplitude of 1.6 V and frequency of 1 Hz. **A** and **B** represents the matrices shown in equation (10) and are dependent on applied voltage, coefficients *a* and *b*. The addition of matrices **A** and **B** is defined as **K**. It is used in the calculation of concentration of oxygen vacancies by Euler's rule.

$C_{(0)}$ is defined as the initial distribution of oxygen vacancies at all nodes. This initial density profile shown in Figure 4.4.1. The density of oxygen vacancies near interface region is varying from 10^{20} to 10^{21} cm^3. This profile is directly taken from the code in Appendix 2.2. Having all the parameters needed to approximate the concentration of oxygen vacancies at all nodes for next time steps, Euler's rule was used. The time step for calculation of concentration of oxygen vacancies was 0.002. But the concentration profile was plotted at only few time intervals as the profile was varying infinitesimally at every time step.

To calculate the current density i.e. the flux of oxygen vacancies which was dependent on the concentration gradient, semi discretization of the one dimensional TiO_2 layer was considered. The one-dimensional space was discretized in *N* number of grid cells, where the edges of the cells were the nodes used to calculate the concentration of oxygen vacancies and the center of the cells were the nodes used to calculate the current density of the oxygen vacancies. Here, **P** is the matrix which represents the behavior dependent on the drift current while **Q** is the matrix which represents the behavior dependent on the diffusion current. **P** and **Q** represent the matrices shown and are

dependent on applied voltage having coefficients *a1* and *b1* respectively. The addition of matrices **P** and **Q** is defined as **R**. The matrix **R** is used in the calculation of flux of oxygen vacancies at all nodes. The flux of the vacancies at all nodes at every time step was defined by the *J* and *Jp* is the flux profile of oxygen vacancies at few intervals.

Then the flux of a node 'x' was plotted vs time at every time step. For the same node '*x*' the graph of current density vs voltage was plotted.

4. Results and Discussion

4.1. Variation of Oxygen ions

This Section includes the graphical data produced from the codes in Appendix 1. Various cases are simulated by varying the boundary conditions and the dependence of the boundary conditions on applied voltage. Flux of oxygen ions coming from the TiO_{2-x} electrolyte layer due to the electrochemical reaction taking place at the interface was considered as the boundary condition. Prior to that, simpler cases were considered to validate the model. Each line signifies concentration at a succeeding time step.

Case 1:

The Flux at both ends was kept zero and the initial concentration of oxygen ions was $1cm^{-3}$,

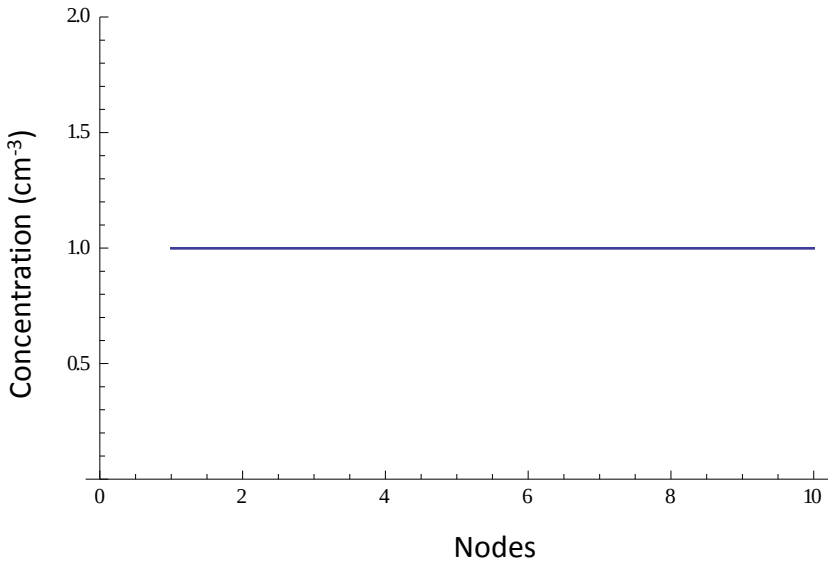

Figure 4.1.1. Initial Concentration of Oxygen Ions

As absence of electric field was expected in the electrodes, the variation of oxygen ions was dependent solely on diffusion. Thus, when there was absence of concentration gradient, the concentration remained the same even after the model was simulated for longer period of time.

Case 2:

The Flux at both ends was kept zero and the initial profile is constantly increasing with distance.

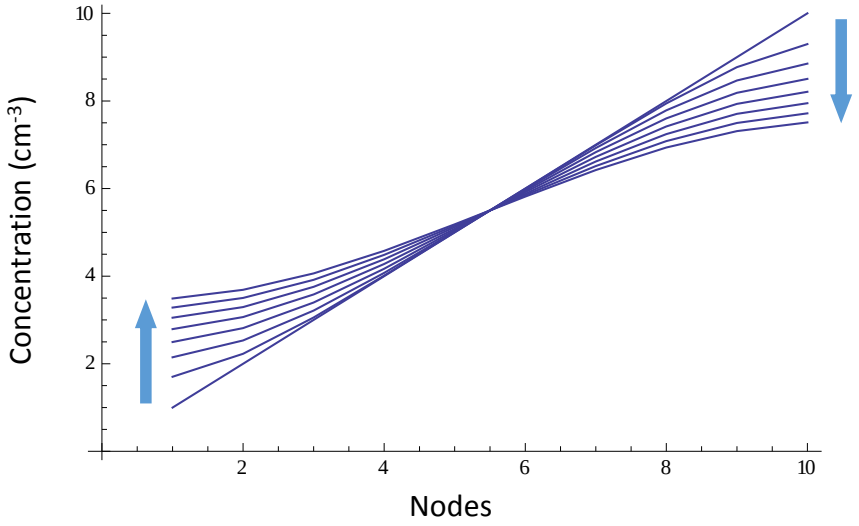

Figure 4.1.2. Trend of Concentration with distance

Due to absence of electric field in the electrodes, the variation of oxygen ions was dependent solely on diffusion. This is a case where the concentration gradient was constant along the distance and thus, the oxygen ions were seemed to move from higher concentration regions to lower concentration regions a constant profile of concentration was observed after longer period of time.

These two cases were used to validate the method. Then the model was used to determine the variation of oxygen ions in the electrodes. The initial concentration of oxygen ions was assumed to be zero because the Pt electrodes were considered to be pure and oxygen ions were introduced by the electrochemical reaction at the interface. The electrochemical reaction was dependent on the voltage and also its polarity.

Case 3:

The flux at the Pt/TiO_{2-x} interface i.e. the flux at the right most node of the left electrode depends on the exponential of the applied voltage, where the voltage varies with time as shown and the initial concentration was assumed to be zero.

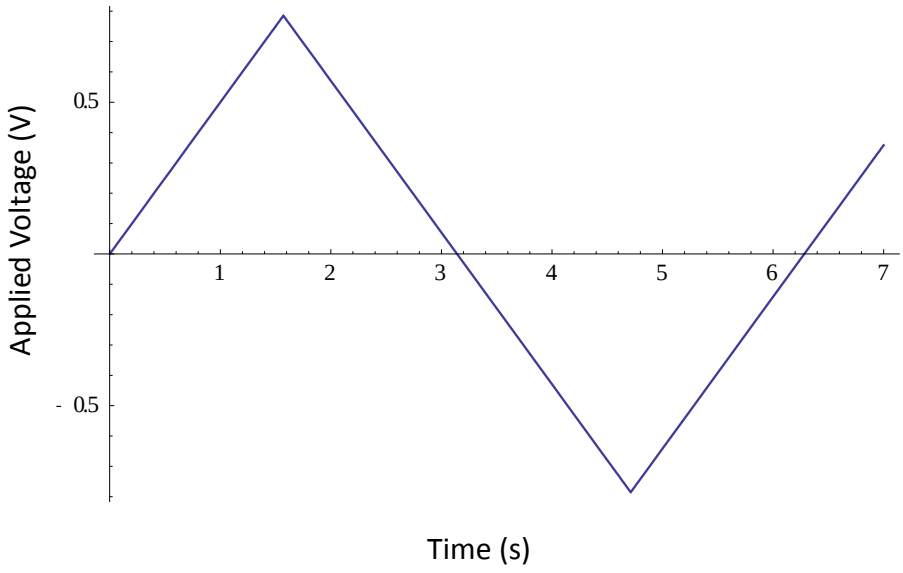

Figure 4.1.3. Trend of Applied Voltage vs Time

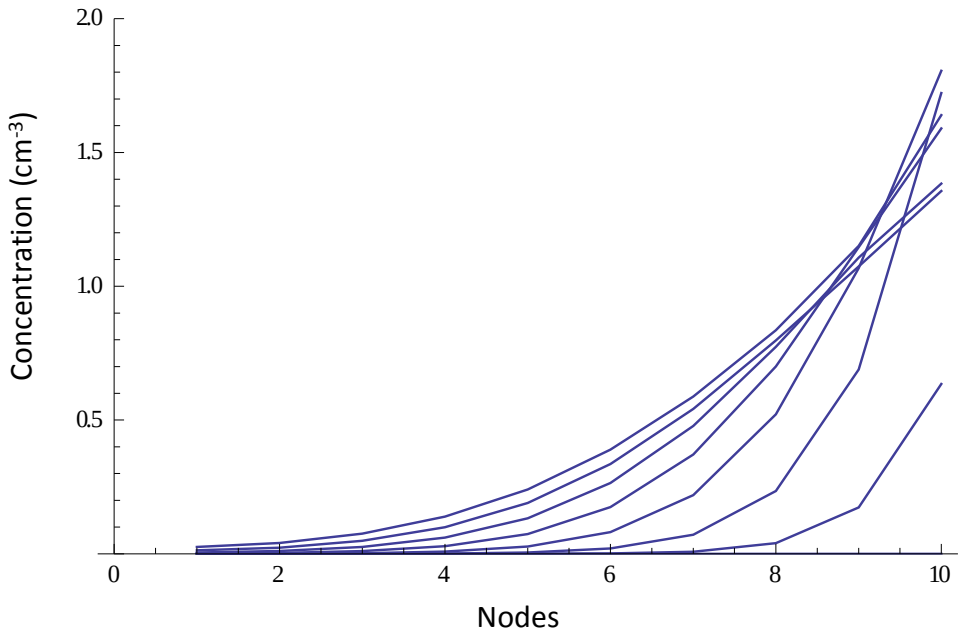

Figure 4.1.4. Trend of Concentration at each node for left electrode

It can be observed from the Figure 4.1.4 that, as the voltage of the cell increases with time, oxygen ions are introduced in the electrode due to the electrochemical reaction taking place at the interface, thus increasing the concentration of oxygen ions. Similarly during the second half the applied voltage cycle, when a negative voltage is applied the concentration of the oxygen ions is reducing but with a gentler pace. The decrease in the ions can be attributed to the fact oxygen gas evolved from the cell. Moreover, absence of electric field was expected in the electrodes, thus the variation of oxygen ions was dependent solely on diffusion. We can clearly see the steady increase of concentration of oxygen ions in the left most node of the electrode which is due to the diffusion of oxygen ions entering at the interface towards the other end of the electrode having lower concentration of oxygen ions.

A graph for the right electrode is also calculated with the same parameters where the leftmost node is at the interface with varying boundary conditions while the rightmost

node has the boundary condition as zero. As the similar reaction will take place at the cathode as well as anode, a similar behavior of the variation of oxygen vacancies was observed in the right electrode as seen in the left electrode.

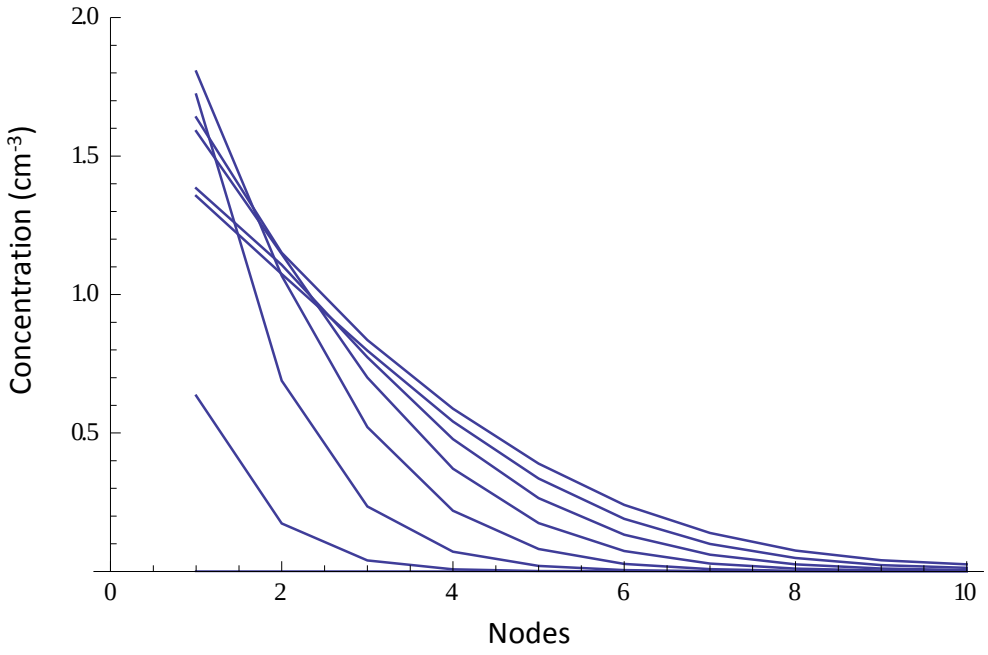

Figure 4.1.5 Trend of Concentration at each node for right electrode

4.2. Variation of oxygen vacancy

This Section includes the graphical data produced from the codes in Appendix 2.1 and 3.1. The codes were written to plot the on the variation of oxygen vacancies in the TiO_{2-x} layer which is dependent on the voltage and then depending on the variation of oxygen vacancies the dependence of flux on voltage was derived. Four graphs showing the variation of concentration of oxygen vacancies with respect to time at

every node, the variation of flux of oxygen vacancies with respect to time at every node, the variation of flux of oxygen vacancies with respect to time at a single node, the variation of flux of oxygen vacancies with respect to voltage at a single node were plotted for every case. The last two graphs were plotted for the left most node of the TiO_{2-x} layer. All four graphs are shown below for one case to discuss in depth of the variation of concentration and the flux of oxygen vacancies in the TiO_{2-x} layer and validate the code based on the mechanism explained in the paper (Jeong et. al.) [1].

The Figure 4.2.1 shows the plot of initial vacancy distribution of oxygen vacancies in the TiO_{2-x} layer which is formed due to the alternating electroforming voltage applied. Here, we can see that the concentration at the near interface region was assumed to be higher than the bulk as mentioned in the Section (3). Moreover the initial concentration of oxygen vacancies was not symmetrical showing highest density of $10^{21}/cm^3$ at the left most node while that of $10^{22}/cm^3$ at the right most node.

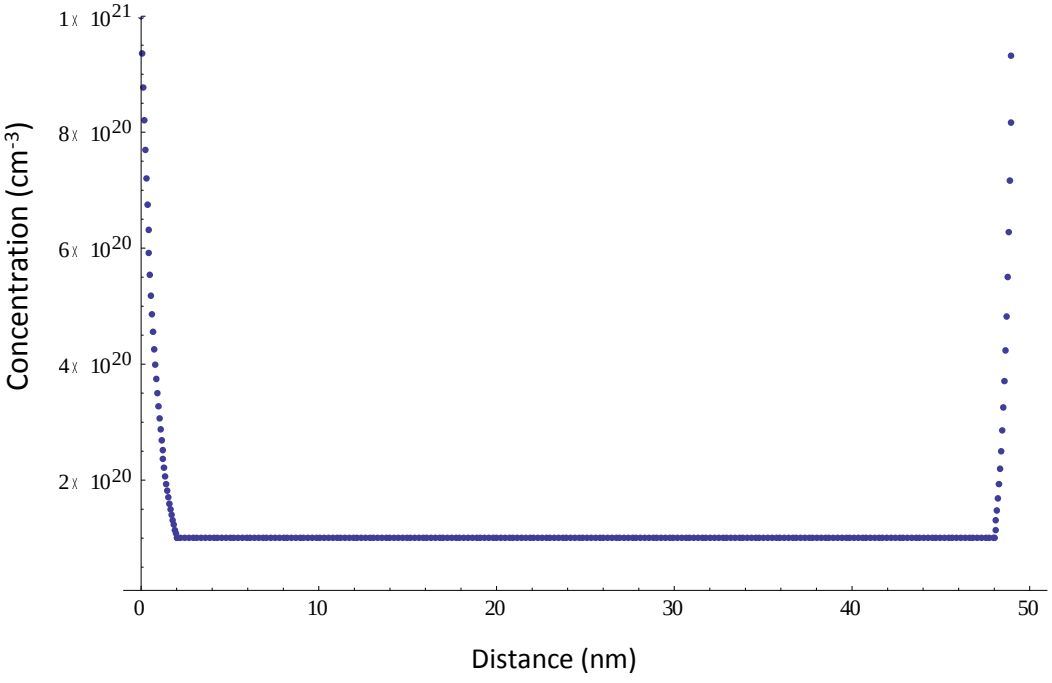

Figure 4.2.1 Initial density profile of oxygen vacancies

This initial density profile of oxygen vacancies was assumed and the simulation was performed. The Figure 4.2.2 shows the applied voltage cycles. All the graphs for a case where the frequency of applied voltage was 1 Hz are plotted below. The voltage cycles are plotted against time step rather than the time. The graph shows applied voltage variation with respect to time. Thus the maximum time for which the model was simulated is 60 s and the period of each voltage cycle is 6 s. For the total time of 60 s, 10 alternating voltage cycles were applied.

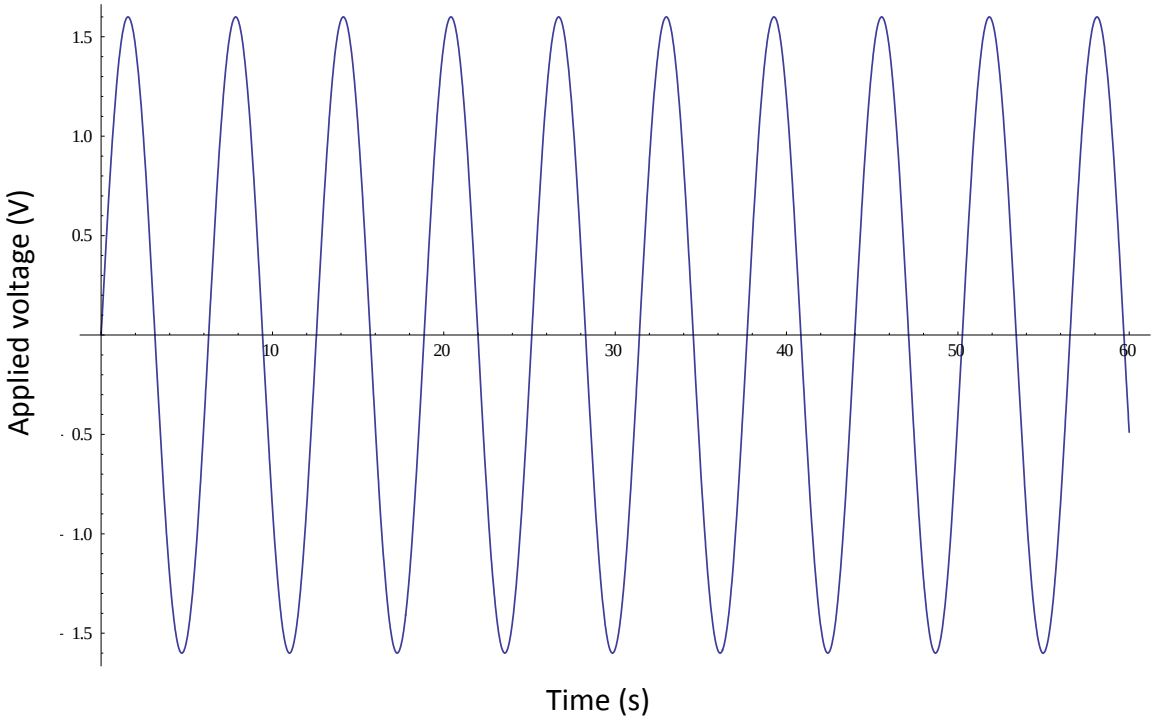

Figure 4.2.2. Voltage (V) vs time (s)

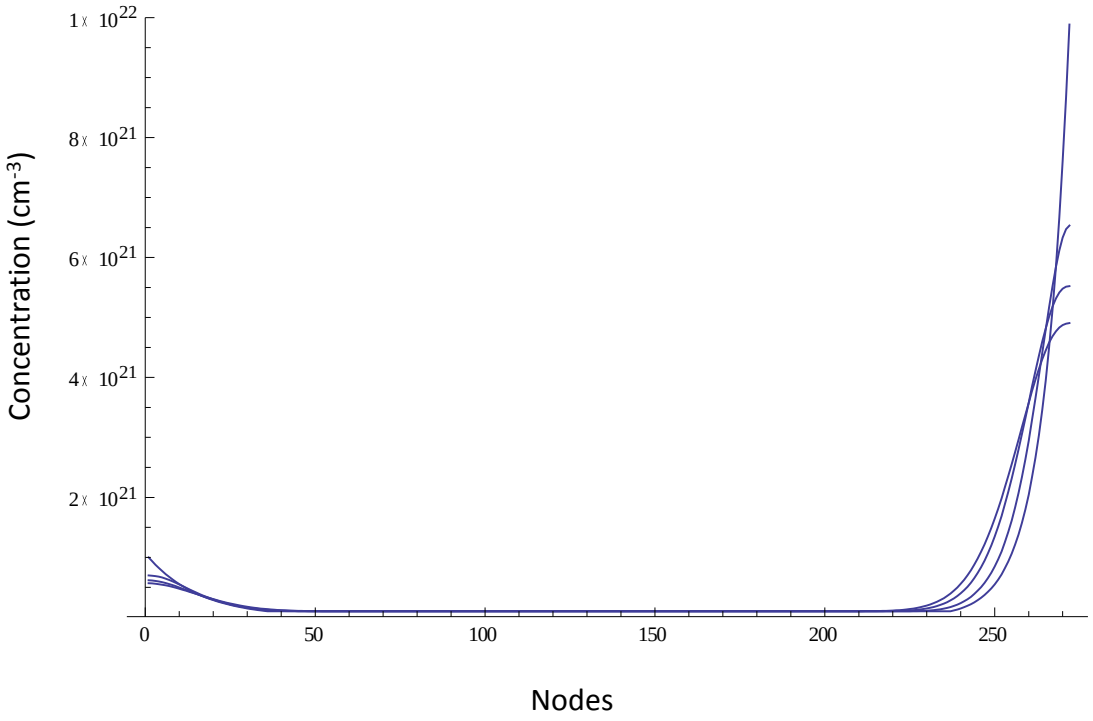

Figure 4.2.3. Concentration vs nodes at times t = 0 s, t = 20 s, t = 40 s and t = 60 s

The Figure 4.2.3 shows the concentraion at every node for times t = 0 s, t = 20 s, t = 40 s and t = 60 s. As we can see that the concentration of oxygen vacancies decreases from the higher concentrations. When only the diffusion is considered the vacancies move from higher concentraion to lower concentraions at much higher rate. But as here both drift and diffusion are takign place and oxygen vacancies are introduced from the interfaces depending on the applied voltages, the movement from higher concentraions to lower concentraions is slow. To achieve better understanding of the concentration of oxyegn vacancies near the left interface region the graph was magnified and is shown in Figure 4.2.4.

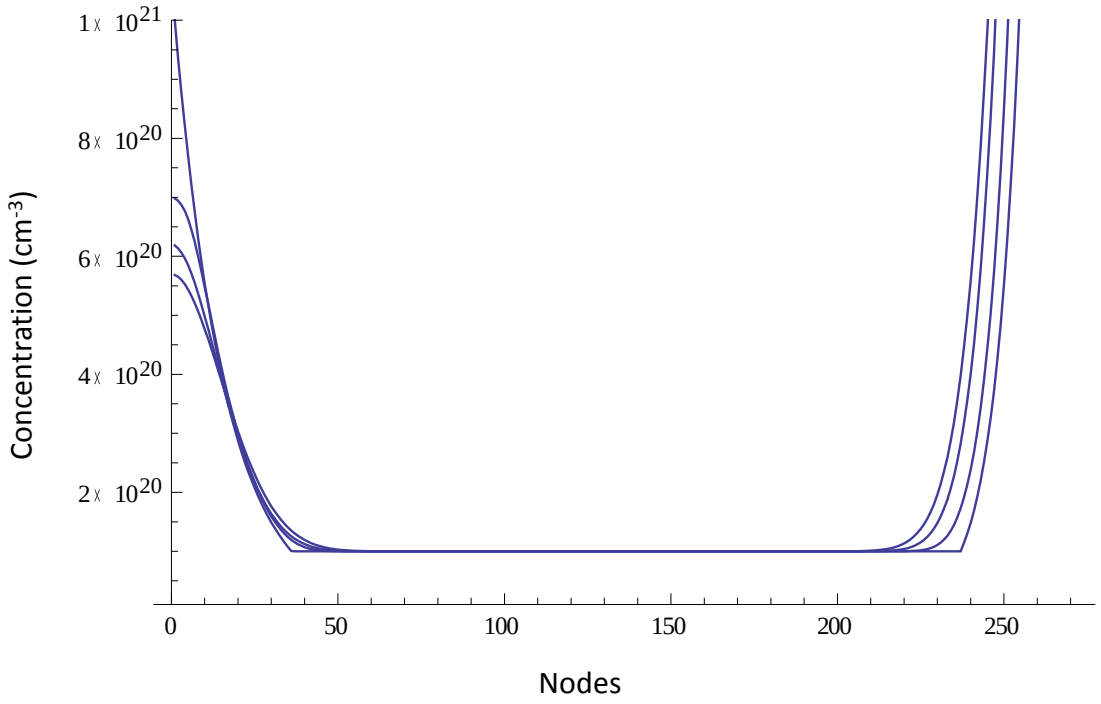

Figure 4.2.4: magnified concentration vs the nodes at times t = 0 s, t = 20 s, t = 40 s and t = 60 s

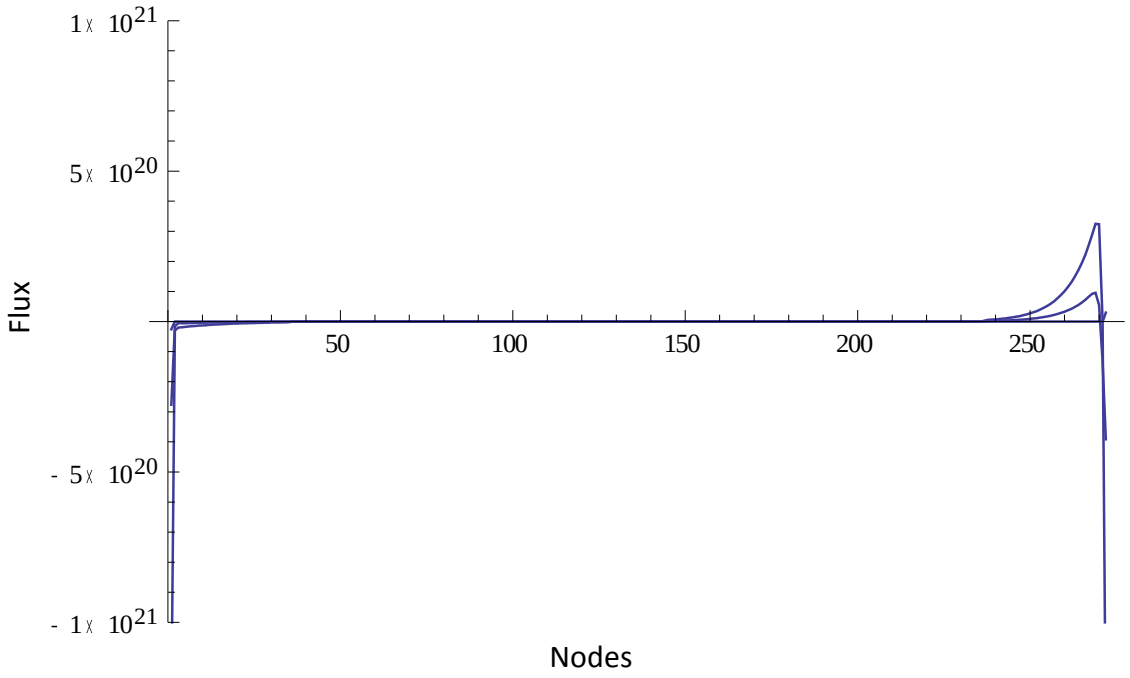

Figure 4.2.5. Flux vs the nodes at times t = 0 s, t = 20 s, t = 40 s and t = 60 s

The current density i.e. flux at all the nodes was calculated to plot the current density variation depending on the voltage. Figure 4.2.5 shows the flux vs the nodes at each at t = 0 s, t = 20 s, t = 40 s and t = 60 s.

Since the formation and annihilation of oxygen vacancies at near left interface region by applying a negative and positive voltage to the right electrode, the oxygen vacancy variation depending on voltage i.e. the flux depending on voltage was determined at the leftmost node of the TiO_{2-x} layer. The voltage dependent flux variation at the left most node at every time (s), is shown in the Figure 4.2.6. The maximum time for which the model was simulated is 60 s.

In the Figure 4.2.6, we can see a peculiar behavior at larger times. If seen closely, the mark of that behavior starts from the first cycle and increases after few aternating voltage cycles. The flux of oxygen vacancies is increasing as voltage is increasing, and decreasing when the voltage is decreasing, which is attributed to the drift flux depending on the applied voltage. Also, the maximum flux decreases after every cycle. As the flux at larger *t* is low, at the end of each cycle the oxygen vacancies start flowing in opposite direction thus showing a slight positive flux in a negative voltage and when then voltage becomes positve, as the flux is in the same direction, it shows as negative flux till the oxygen vacancies start flowing in the direction of current, when the curve shift to positve flux, thus showing a slight negative flux at the start of each positive cycle. This behaviour becomes prominient after every cycle.

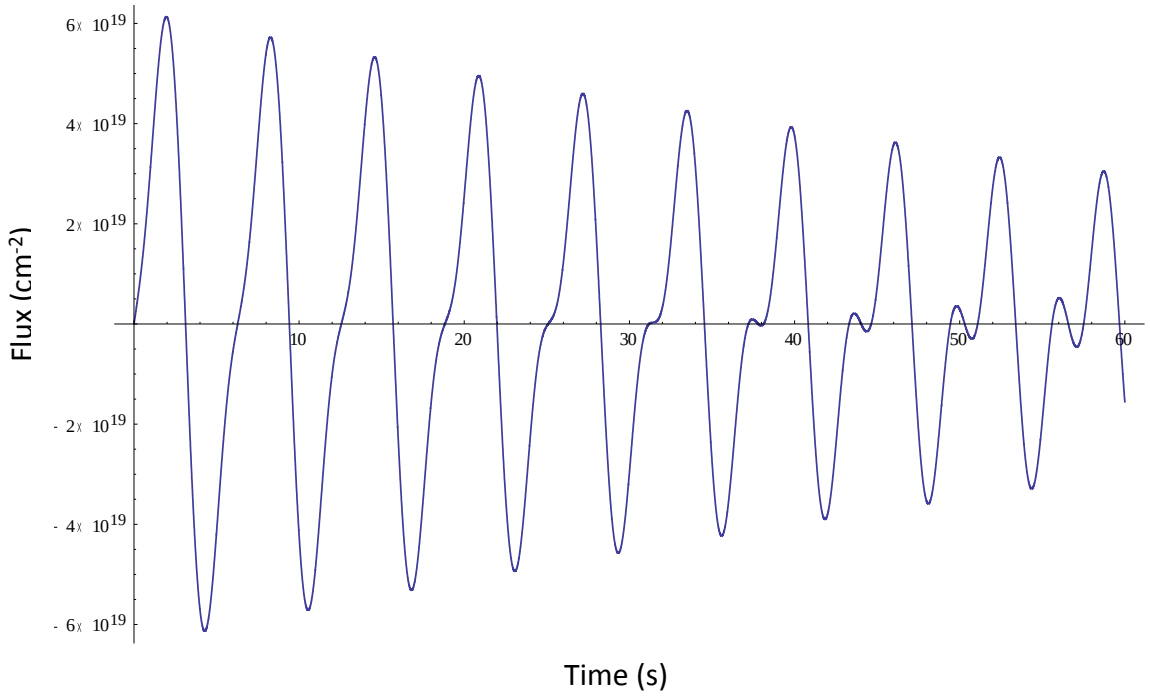

Figure 4.2.6. Flux (J) vs time (s) for the left mode node

Finally, the flux at the left most node was plotted verses applied voltage. This curve can be classified as a characteristic hysteresis curve. The Figure 4.2.7 shows the Flux vs voltage i.e. current density vs voltage at the left most node for 10 cycles of alternating voltage. Figure 4.2.7 shows pinched hysteresis behavior for the J-V curve, illustrating elementary representation of the bipolar switching behavior induced by the anion migration induced mechanism observed in the resistive cell.

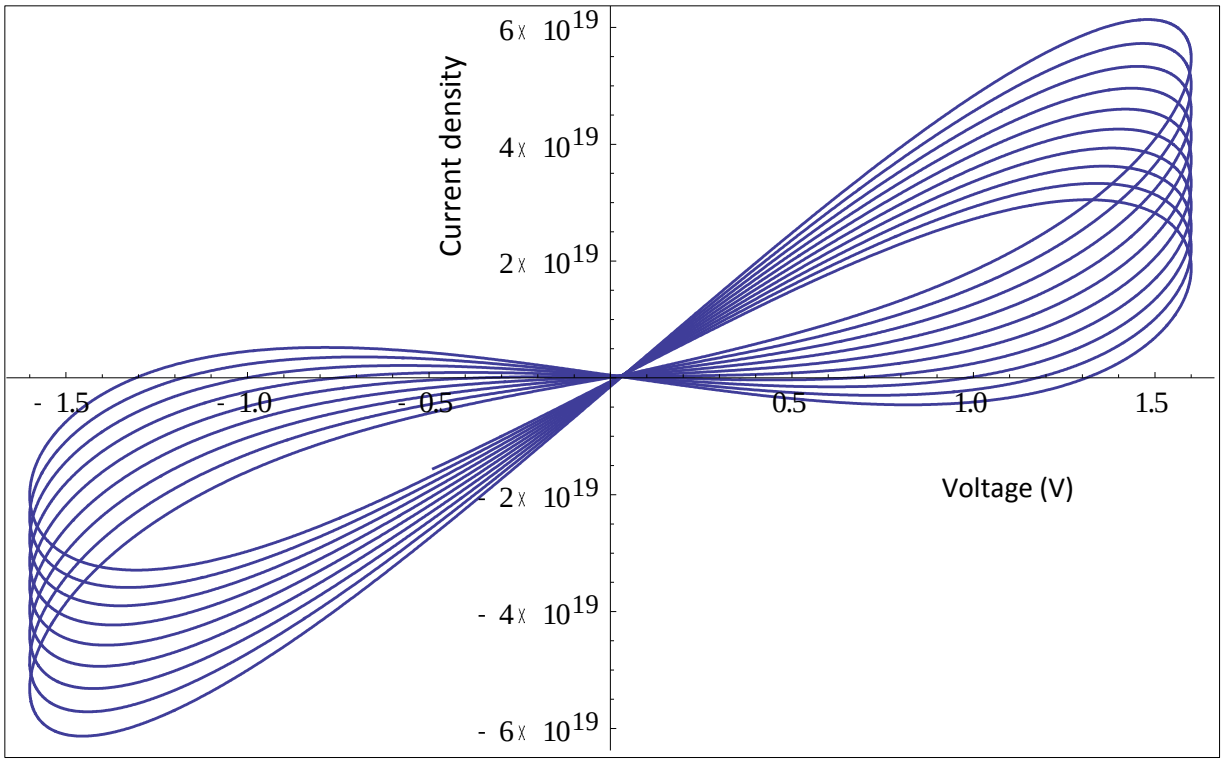

Figure 4.2.7: Flux (J) vs Voltage (V)

4.3. Experimental graphical data

In this Section, the graphs from an experimentation are plotted. The values obtained from the experiment are displayed in Table 3.4. The applied voltage cycle is shown in the Figure 4.3.1. It is clear that the frequency of the alternating voltage cycle applied was low. From the data provided the equation of the curve was calculated and found to be

$$V = 1.6 * \sin[0.00216 * t + 0.0618]$$

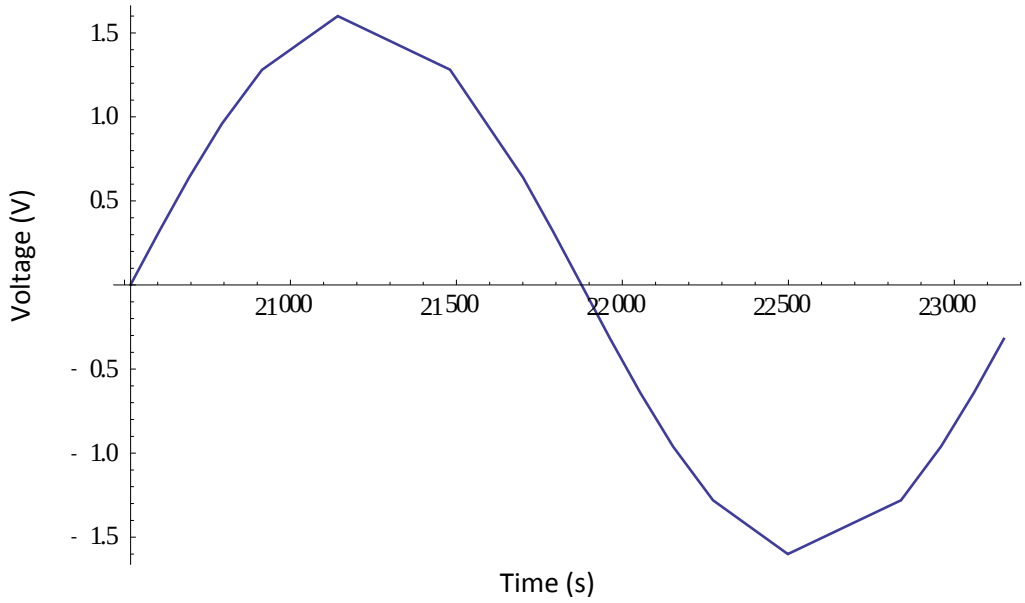

Figure 4.3.1 Voltage (V) vs time (s)

By applying the voltage, current was noted and the *I-V* curves are plotted below. The non-linear pinched hysteresis behavior was observed. To understand the behavior clearly, two graphs magnifying the positive and negative *I-V* curve are plotted in different graphs. It can be observed that the self-intersection point is shifted towards the positive voltage and the hysteresis behavior was obtained after longer time periods. Also, it can be observed that the current reaches higher values in the positive voltage cycle while limits to smaller values during the negative voltage cycles.

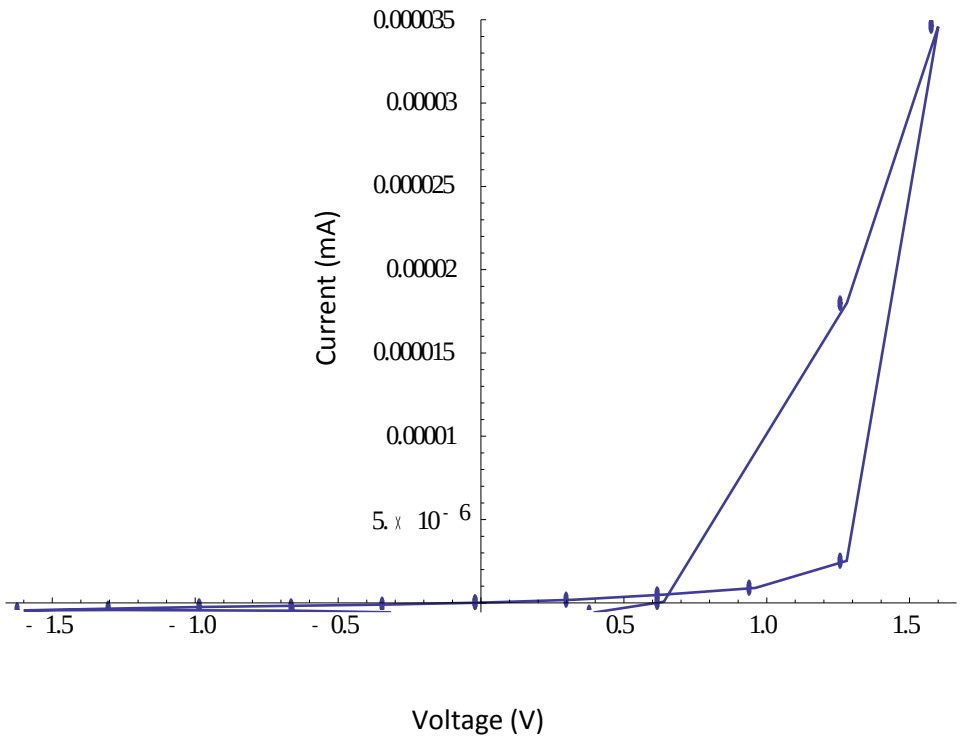

Figure 4.3.2: Current vs Voltage magnifying the positive voltage cycle

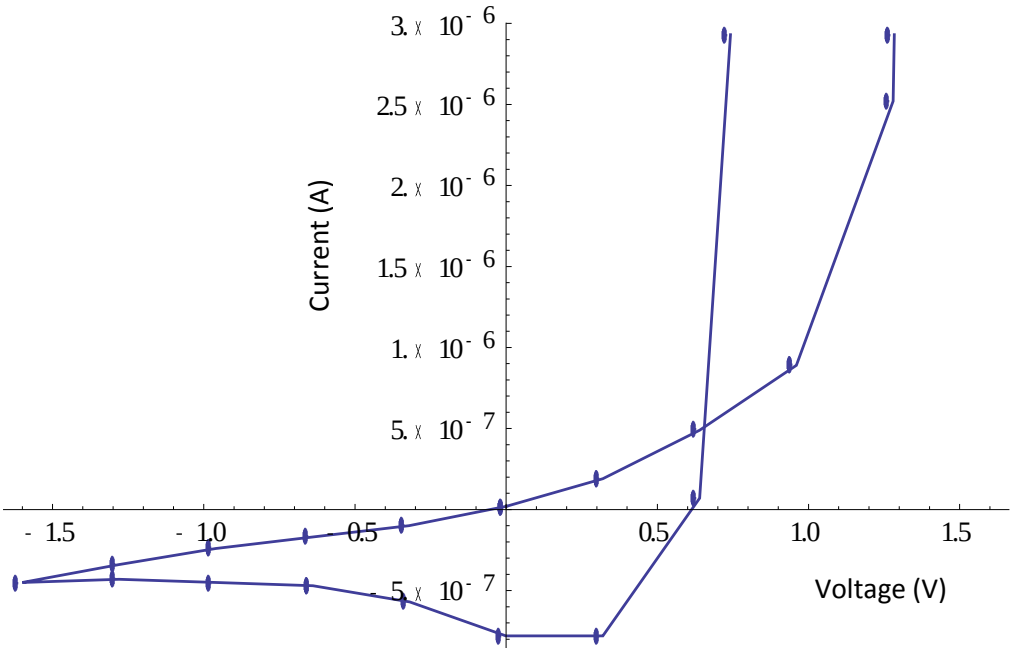

Figure 4.3.3: Current vs Voltage magnifying the negative voltage cycle

4.4. Simulated J -V curves for experimental data

This Section includes the graphical data produced from the codes in Appendix 2.2 and 3.2. A simplification of the model was done to simulate the code for lower frequencies as well as the longer time periods in order to compare the graphical data resulted from the simulation to the experimental graphical data. The initial concentration of oxygen vacancies was assumed to be symmetrical and the number of nodes were very less as compared to the previous model. The codes were written to plot the on the variation of oxygen vacancies in the TiO_{2-x} layer which is dependent on the voltage and then depending on the variation of oxygen vacancies the dependence of flux on voltage was derived. Four graphs showing the variation of concentration of oxygen vacancies with respect to time at every node, the variation of flux of oxygen vacancies with respect to time at every node, the variation of flux of oxygen vacancies with respect to time at a single node, the variation of flux of oxygen vacancies with respect to voltage at a single node were plotted for every case. The last two graphs were plotted for the left most node of the TiO_{2-x} layer. Only the graphs representing the variation of the flux of oxygen vacancies dependent on the applied voltage are shown below for different frequencies of the applied voltage to discuss in depth the variation of the current density with the change in the frequency of the applied voltage.

The following Figure 4.4.1 shows the plot of initial vacancy distribution of oxygen vacancies in the TiO_{2-x} layer which is assumed to be formed due to the alternating electroforming voltage applied. Here we can see that the concentration at the near interface region was assumed to be higher than the bulk as mentioned in the Section (3).

Moreover, the initial concentration of oxygen vacancies was symmetrical showing highest density of $10^{21}/cm^3$ at the near interface regions while that of $10^{20}/cm^3$ in the bulk.

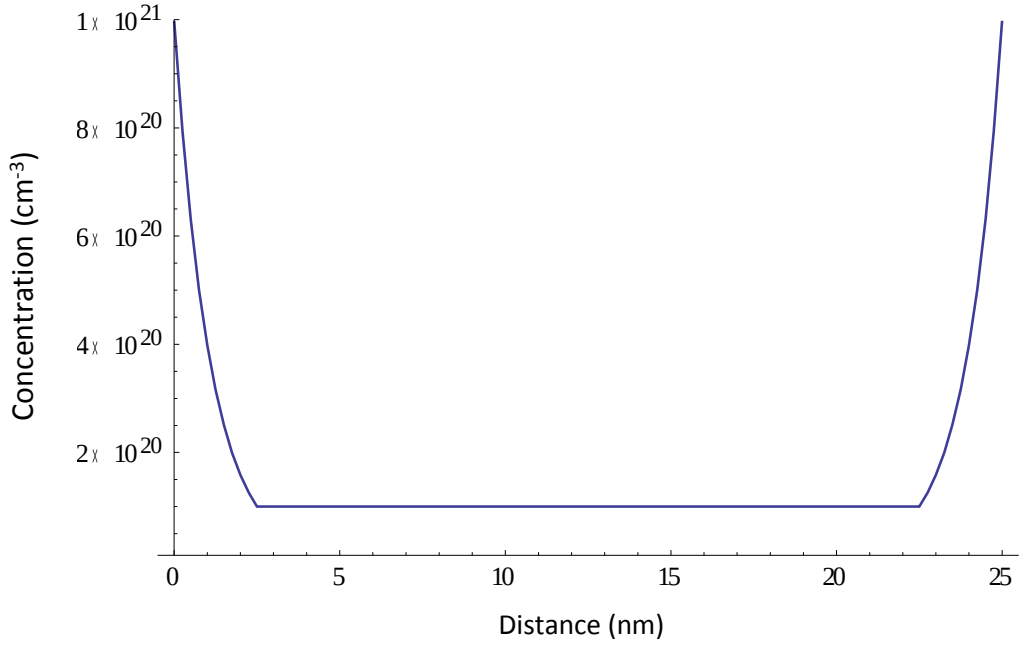

Figure 4.4.1: Initial concentration of oxygen vacancies

With the assumption that, the initial profile of oxygen vacancies was as shown in the Figure 4.4.1, the code shown in Appendix 3.2 was simulated for frequencies as f = 0.25 Hz, f = 0.5 Hz, f = 1 Hz, f = 2 Hz, f = 4 Hz of the applied voltage and only the graphs showing variation of oxygen vacancies flux with respect to voltage are plotted below.

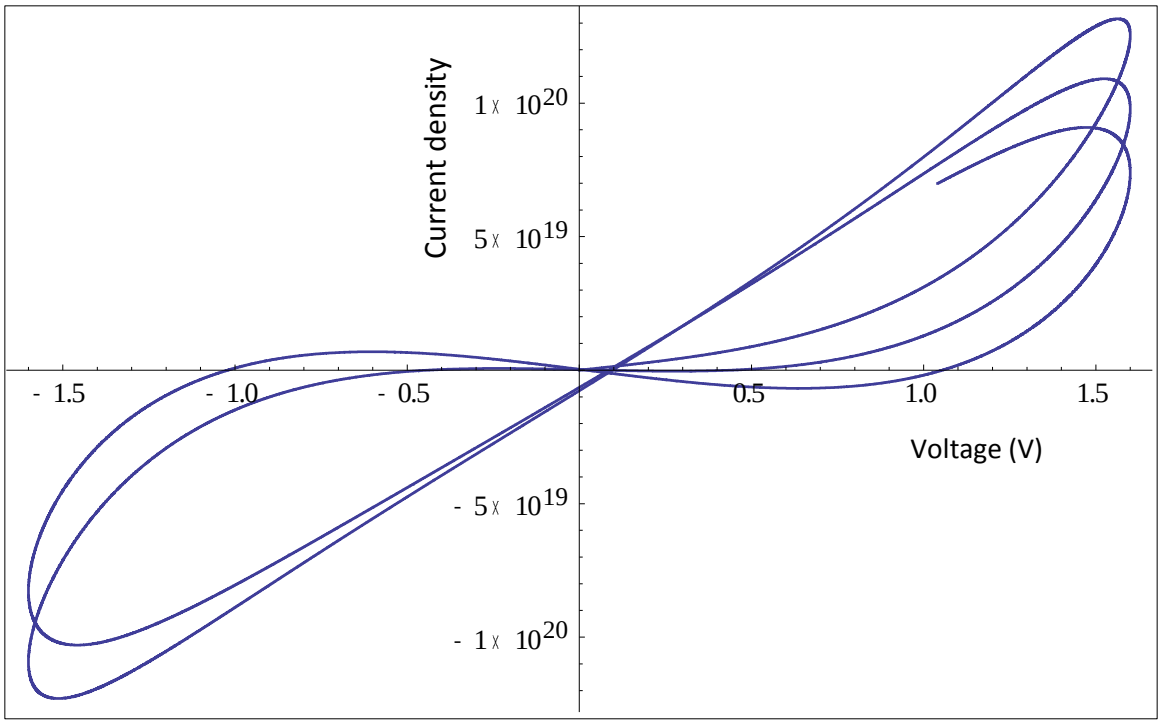

Figure 4.4.2: J -V curve for applied voltage frequency of 0.25 Hz

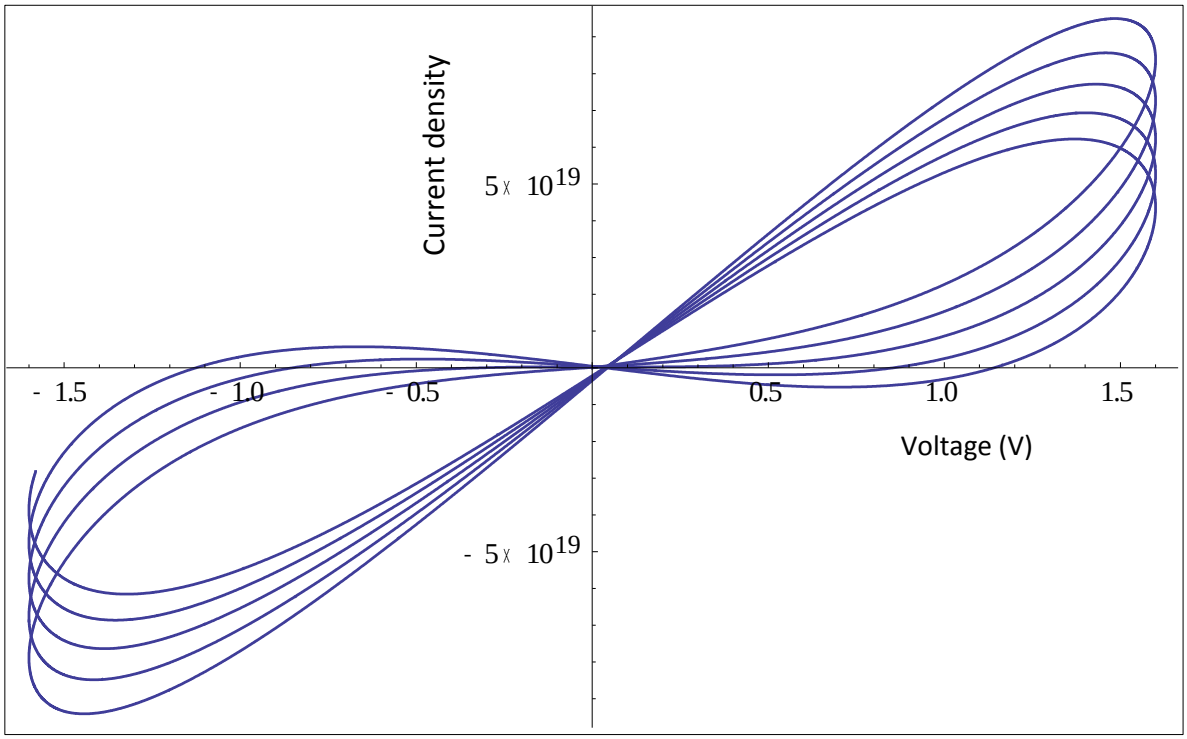

Figure 4.4.3: J -V curve for applied voltage frequency of 0.5 Hz

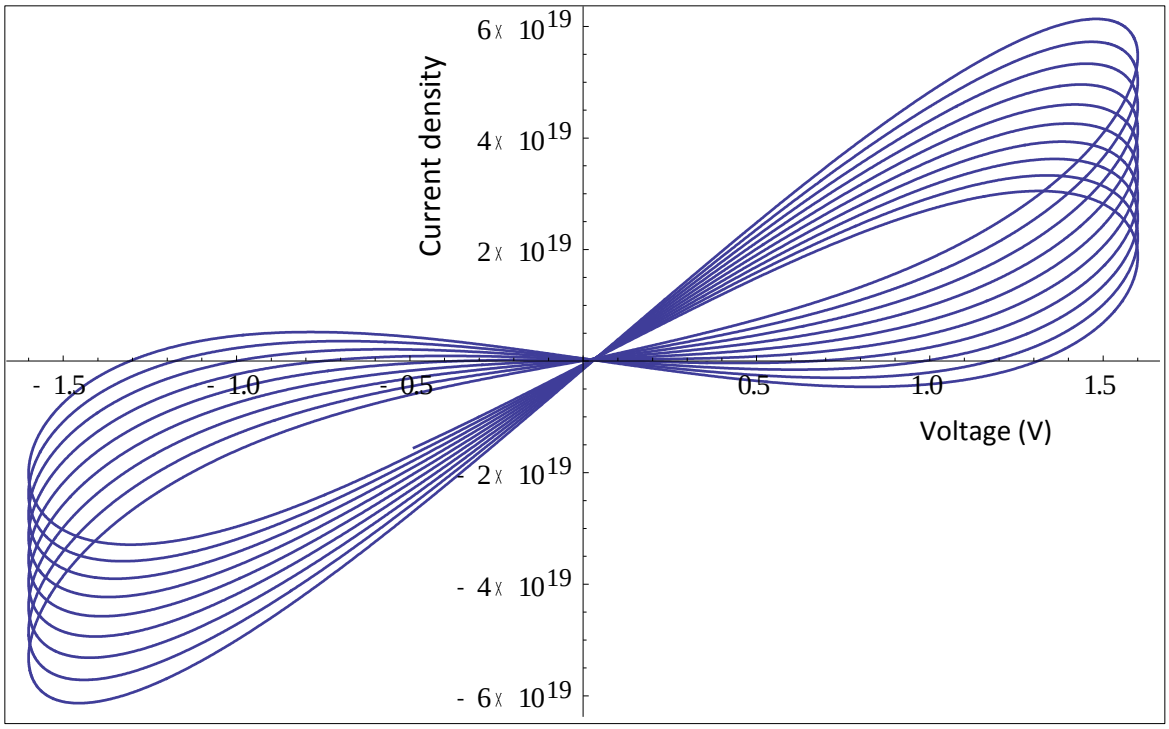

Figure 4.4.4: J -V curve for applied voltage frequency of 1 Hz

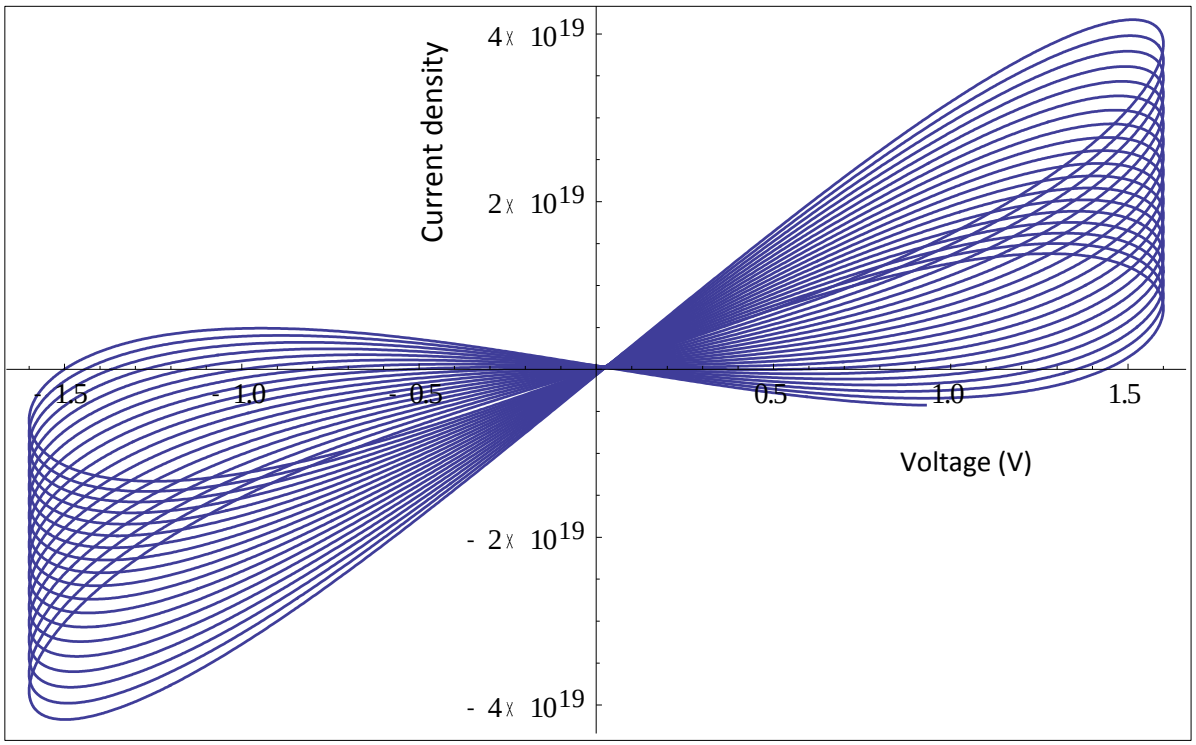

Figure 4.4.5: J -V curve for applied voltage frequency of 2 Hz

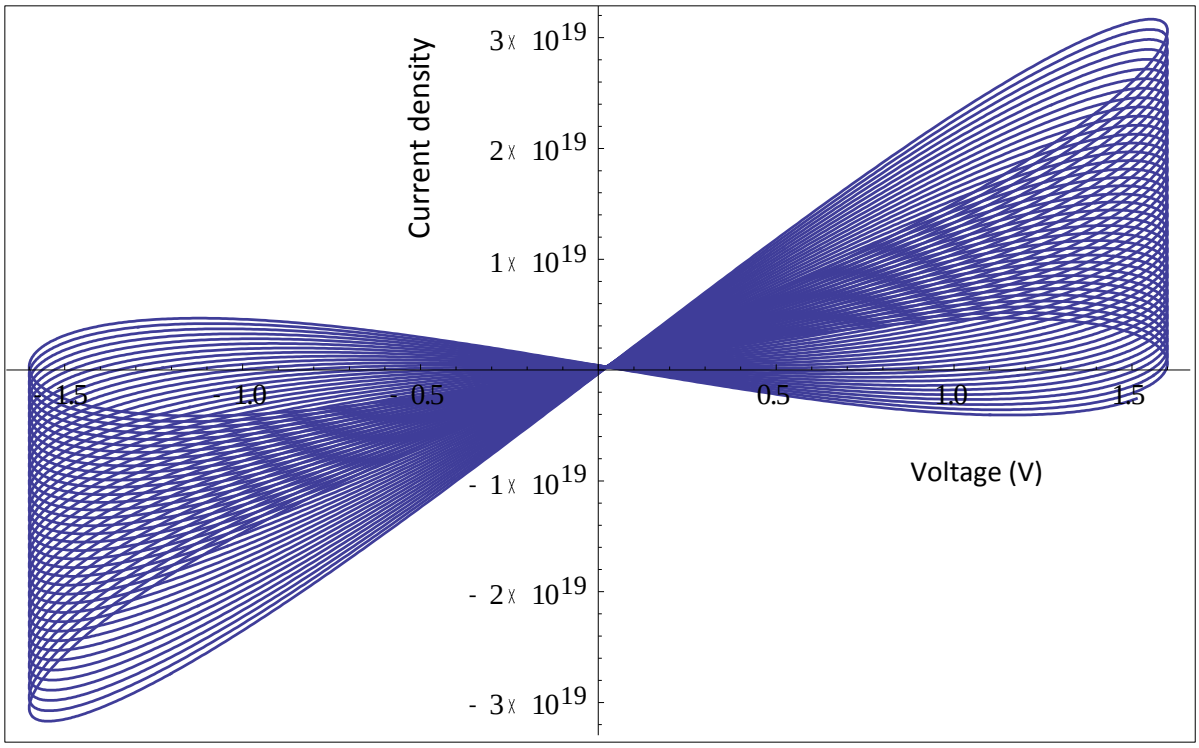

Figure 4.4.6: J -V curve for applied voltage frequency of 4 Hz

It can be observed from the above graphs that the J-V curves are rotating around the self-intersection point. As the applied voltage is alternating between positive and negative values, the flux decreases when the voltage completes one cycle. The decrease in flux is attributed to the decrease in the diffusion flux because of decrease in oxygen vacancies at the left most node along with time. This decrease in flux which can be clearly seen in the flux vs time graph is represented as the turning of the flux vs voltage graph.

Moreover, it can also be observed that the curves are rotating faster at higher frequencies. At higher frequencies, the current cycle is changing faster which is causing the fast turns of the flux as shown in the Figure. As after every cycle the flux decreases

by some percentage, so at higher frequencies there are more number of voltage cycles for the time span than for the lower frequencies. Thus, the graph at higher frequencies if turning faster than the lower frequencies.

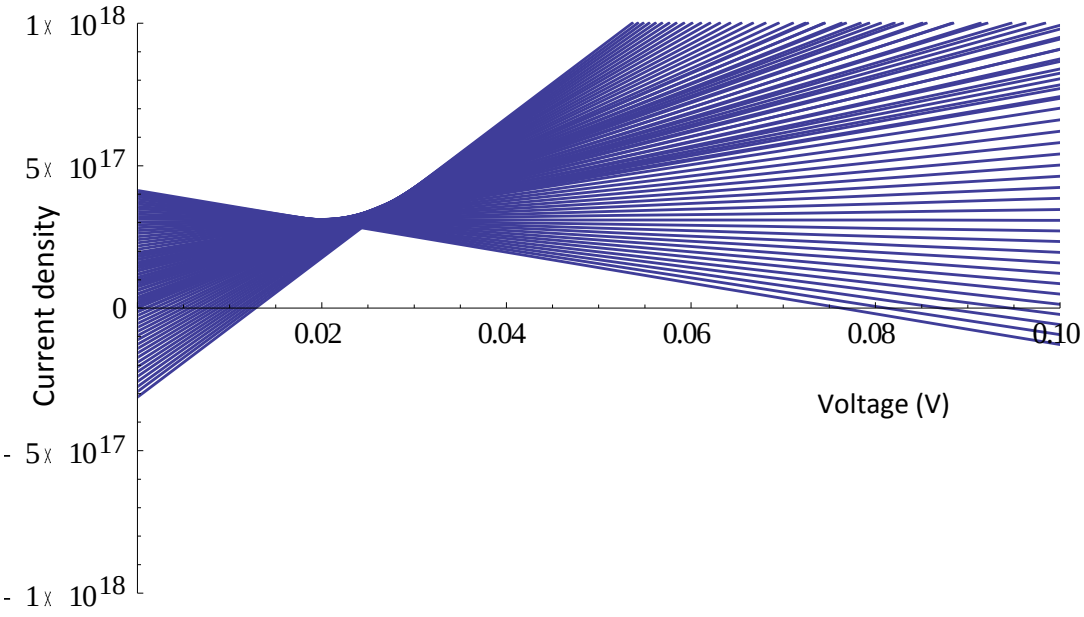

Figure 4.4.7: magnified J -V curve for applied voltage frequency of 4 Hz

As the frequency of the applied voltage cycle is reducing, a different shape of the *J-V* curves can be observed. The curve inclines to non-linearity at the frequency of 0.25 Hz and it can be attributed to the slow buildup of oxygen vacancies. The Figure 4.4.2 shows the non-linearity in the curve. This model can be used to qualitatively explain the nonlinear pinched hysteresis behavior of experimental data at lower frequency of the applied voltage.

The self-intersection point is shifted for all the *J-V* curves as seen in the experimental results. However, it has shifted less at higher frequencies because the variation in the concentration of oxygen vacancies is faster at higher frequencies. The shift in self-intersection point for the highest frequency of 4 Hz is shown in the Figure 4.4.7. The self-intersection point for lowest frequency is at about 0.1 V while that of highest frequency is at 0.02 V.

The drift of pinched hysteresis graph for the flux verses voltage profile at applied voltage frequency of 4 Hz is shown in the Figure 4.4.8. It only includes the flux for certain voltage cycles specifying the significance of rotation of the plot.

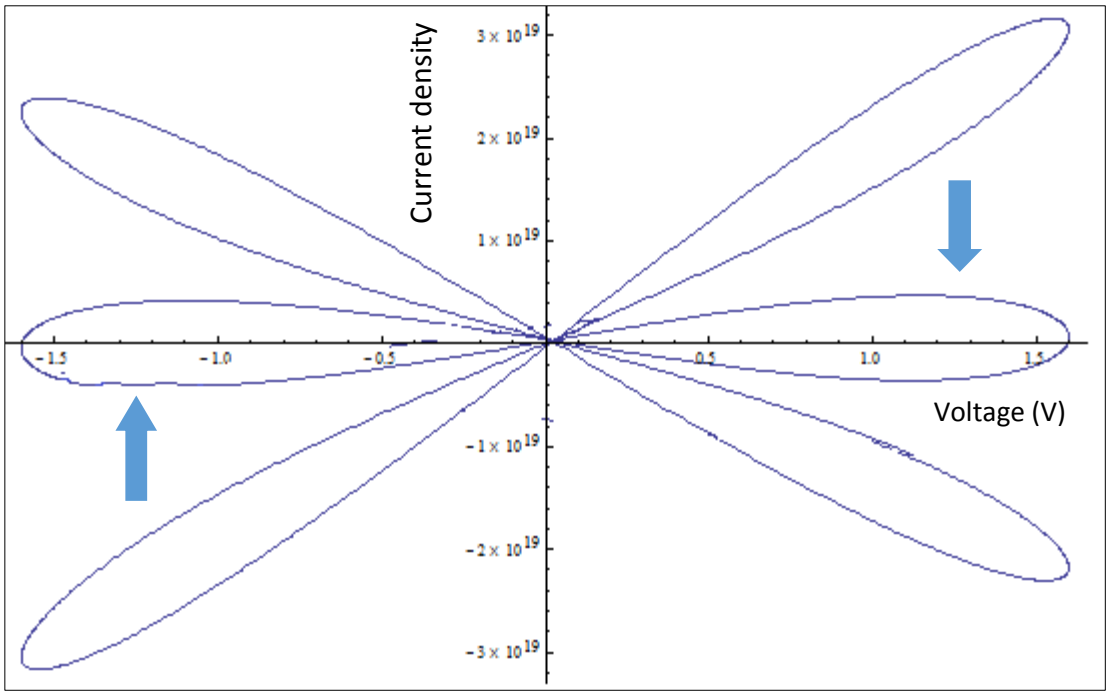

Figure 4.4.8: Drift of the pinched hysteresis of the J -V curve for applied voltage frequency of 4 Hz

5. Conclusion

The electric conduction behavior in $Pt/TiO_2/Pt$ switching cells was modeled for bipolar resistive switching (BRS) mechanism. The characterized conduction behavior was interpreted in terms of the oxygen ions/vacancies migration due to the drift-diffusion.

A generic model was created to calculate the distribution of oxygen vacancies and oxygen ions in the TiO_2 electrolyte and the Pt electrode respectively. The flux of oxygen vacancies was also modelled and calculated to study its behavior with respect to applied voltage. The main accomplishment was to achieve a pinched hysteresis behavior of J-V curves qualitatively explaining the bipolar resistive switching mechanism.

This model was then modified and used to simulate the results obtained from experimental data. The simulated results were compared with experimental data to derive an understanding of the mechanism in the experimental resistive cell. The simulated graphs at lower frequencies of applied voltage had a characteristic nonlinear pinched hysteresis behavior. The self-intersection of the simulated J-V curves was shifted from the origin as seen in the experimental results. The assessment shows slight deviation in the simulated results as compared to experimental results and the deviation is caused due to certain assumptions taken during the simulation. Extension of this model including the clarification of assumptions and calculation at even lower frequency of applied voltage can lead to better approximation of the *I-V* curve obtained by experimental results.

The variation in behavior of flux of vacancies with respect to the frequency of the applied voltage in the simulated *J-V* curves was also studied. The results obtained showed

that the flux was decreasing after every voltage cycle. Also the decrease in flux is faster in higher frequencies than lower frequencies.

Application of this model to the mechanism of bipolar resistive switching can be accomplished by including more detailed analysis of the distribution of space charges and their effect on the electrical conductance, along with the distribution of oxygen vacancies in the electrolyte.

6. Appendix 1

1.1. Mathematica code to calculate the oxygen ions in the left electrode

```
f=1;M=3500;m=10;dM= 500;
V=Table[0.5* ArcSin[Sin[f*0.002*n]],{n,0,M}];
Vp=Plot[0.5* ArcSin[Sin[f*0.002*n]],{n,0,M}]
B=SparseArray[{{1,1}→-1,{m,m}→-1,Band[{2,2},{m-1,m-1}]→-
2,Band[{2,1}]→1, Band[{1,2}]→1},{m,m}]
G =Table[Normal[SparseArray[{{m,1}→Exp[0.5*
ArcSin[Sin[f*0.002*n]]]},{m,1}]],{n,0,M}];
cm[0]= ConstantArray[0,m];
Do[cm[n+1] = cm[n] + 0.002B.cm[n] + 0.002G〚n+1〛,{n,0,M-1}]
Do[cm[n],{n,500,M,dM}] ;
Do[Print[Show[Table[ListLinePlot[Flatten[cm[n]],PlotRange→{0,2.7}],{n,0,
M,dM}]]]]
```

1.2. Mathematica code to calculate the oxygen ions in the right electrode

```
f=1;M=3500;m=10;dM= 500;
V=Table[0.5* ArcSin[Sin[f*0.002*n]],{n,0,M}];
Vp=Plot[0.5* ArcSin[Sin[f*0.002*n]],{n,0,M}]
B=SparseArray[{{1,1}→-1,{m,m}→-1,Band[{2,2},{m-1,m-1}]→2,Band[{2,1}]→1,
Band[{1,2}]→1},{m,m}]
G =Table[Normal[SparseArray[{{1,1}→Exp[0.5*
ArcSin[Sin[f*0.002*n]]]},{m,1}]],{n,0,M}];
cm[0]= ConstantArray[0,m];
Do[cm[n+1] = cm[n] + 0.002B.cm[n] + 0.002G〚n+1〛,{n,0,M-1}]
Do[cm[n],{n,500,M,dM}] ;
Do[Print[Show[Table[ListLinePlot[Flatten[cm[n]],PlotRange→{0,2.7}],{n,0,
M,dM}]]]]
```

7. Appendix 2

2.1. The code for initial density profile of oxygen vacancies

```
nodes1 =Table[j,{j,0,2,0.057}];
nodes2 =Table[j,{j,2,48,0.231}];
nodes3 =Table[j,{j,48,50,0.057}];
nodes=Join[nodes1,nodes2,nodes3];
den1=Table[{10^21*10^-0.5x},{x,nodes1}];
den2=Table[{10^20},{x,nodes2}];
den3=Table[{10^20*10^x-48},{x,nodes3}];
denp1=Table[{x,10^21*10^-0.5x},{x,nodes1}];
denp2=Table[{x,10^20},{x,nodes2}];
denp3=Table[{x,10^20*10^x-48},{x,nodes3}];
den=Join[den1,den2,den3];
denp=Join[denp1,denp2,denp3];
ListPlot[denp, PlotRange→{10^19,10^21}]
```

2.2. The code for initial density profile of oxygen vacancies for experimental results

```
den1=Table[{10^21*10^-0.4x},{x,0,2.5,0.25}];
den2=Table[{10^20},{x,2.75,22.25,0.25}];
den3=Table[{10^20*10^0.4(x-22.5)},{x,22.5,25,0.25}];
den=Join[den1,den2,den3];
denp1=Table[{x,10^21*10^-0.4x},{x,0,2.5,0.25}];
denp2=Table[{x,10^20},{x,2.75,22.25,0.25}];
denp3=Table[{x,10^20*10^0.4(x-22.5)},{x,22.5,25,0.25}];
Eden=Join[den1,den2,den3];
Edenp=Join[denp1,denp2,denp3];
ListPlot[Edenp,PlotRange→{10^19,10^21}]
ListLinePlot[Edenp,PlotRange→{10^19,10^21}]
```

8. Appendix 3

3.1. The code for variation of oxygen vacancies depending on the voltage

```
z0=2;μ0=3.87*10^-17;m=272;d0=50*10^-7;D00=10^-18;
x=3;M=3500;f=1;dM=500;q=1.602*10^-19;
a=z0*μ0*(m-1)^2/(2*Subscript[d, 0]^2);
b=D00*(m-1)^2/Subscript[d, 0]^2;
a1=-z0*μ0*(m-1)/(2*d0);
b1=-D00*(m-1)/d0;
V=Table[-0.5* ArcSin[Sin[f*0.002*n]],{n,0,M}];
Vp=Plot[-0.5* ArcSin[Sin[f*0.002*n]],{n,0,M}]
A=Table[a*-0.5*              ArcSin[Sin[f*0.002*n]]*SparseArray[{{1,1}→-
1,{m,m}→1,Band[{2,2},{m-1,m-1}]→0,Band[{2,1}]→-1,
Band[{1,2}]→1},{m,m}],{n,0,M}];
B=b*SparseArray[{{1,1}→-1,{m,m}→-1,Band[{2,2},{m-1,m-1}]→-
2,Band[{2,1}]→1, Band[{1,2}]→1},{m,m}];
K=Table[A[[n+1]]+B,{n,0,M}];
cm[0]=den;
cm+1[0]=0;
Do[cm[n+1]=cm[n]+0.002K[[n+1]].cm[n],{n,0,M-1}];
Do[cm[n],{n,0,M,dM}];
Do[Print[Show[Table[ListLinePlot[Flatten[cm[n]],PlotRange→{10^19,10^21}],{n
,0,M,dM}]]]]
Do[Print[Show[Table[ListLinePlot[Flatten[cm[n]],PlotRange→{10^19,10^22}],{n
,0,M,dM}]]]]
P=Table[a1*-0.5*
ArcSin[Sin[f*0.002*n]]*SparseArray[{{1,1}→2,{m+1,m}→2,Band[{2,2},{m,m}]
→1,Band[{2,1}]→1},{m+1,m}],{n,0,M}];
```

```
Q=b1*  SparseArray[{{1,1}→0,{m+1,m}→0,Band[{2,2},{m,m}]→1,Band[{2,1}]→-
1},{m+1,m}];
R=Table[P[[n+1]]+Q,{n,0,M}];
J=Table[R[[n+1]].cm[n],{n,0,M}];
Jp=Do[Print[Show[Table[ListLinePlot[Flatten[R[[n+1]].cm[n]],PlotRange→{-
10^10,10^10}],{n,0,M,dM}]]]]
Flatten[Transpose[J][[x]]];
ListLinePlot[Flatten[Transpose[J][[x]]]]
ListLinePlot[Partition[Riffle[Table[-0.5*
ArcSin[Sin[f*0.002*n]],{n,0,M}],q*Flatten[Transpose[J][[x]]]],2]]
```

3.2. The code for variation of oxygen vacancies depending on the voltage for experimental results

```
z0=2;μ0=3.87*10^-17; m=101;d0=25*10^-7;D00=10^-18;x=2;M=14000;f=0.25;
a=z0*μ0*(m-1)^2/(2*Subscript[d, 0]^2);
b=D00*(m-1)^2/Subscript[d, 0]^2;
a1=z0*μ0*(m-1)/(2*d0);
b1=D00*(m-1)/d0;
V=Table[1.6* Sin[f*0.002*n],{n,0,M}];
Vp=Plot[1.6* Sin[f*0.002*n],{n,0,M}]
A=Table[a*1.6* Sin[f*0.002*n]*SparseArray[{Band[{2,1}]→-
1,Band[{1,1}]→0, Band[{1,2}]→1},{m,m}],{n,0,M}];
B=b*SparseArray[{Band[{2,1}]→1,Band[{1,1}]→-2, Band[{1,2}]→1},{m,m}];
K=Table[A[[n+1]]+B,{n,0,M}];
cm[0]=Eden;
cm+1[0]=0;
Do[cm[n+1]=cm[n]+0.002K[[n+1]].cm[n],{n,0,M-1}];
Do[cm[n],{n,0,M,500}];
```

```
Do[Print[Show[Table[ListLinePlot[Flatten[cm[n]],PlotRange→{10^19,10^21}],{n
,0,M,500}]]]]
Do[Print[Show[Table[ListLinePlot[Flatten[cm[n]],PlotRange→{10^19,10^22}],{n
,0,M,500}]]]]
P=Table[-a1*1.6* Sin[f*0.002*n]*SparseArray[{Band[{2,1}]→-
1,Band[{1,1}]→0, Band[{1,2}]→1,{1,m}→-1,{m,1}→1},{m,m}],{n,0,M}];
Q=-b1* SparseArray[{Band[{2,1}]→1,Band[{1,1}]→-2,
Band[{1,2}]→1,{1,m}→1,{m,1}→1},{m,m}];
R=Table[P[[n+1]]+Q,{n,0,M}];
J=Table[R[[n+1]].cm[n],{n,0,M}];
Jp=Do[Print[Show[Table[ListLinePlot[Flatten[R[[n+1]].cm[n]],PlotRange→{-
10^20,10^20}],{n,0,M,500}]]]]
ListLinePlot[Flatten[Transpose[J][[2]]]]
ListLinePlot[Partition[Riffle[Table[1.6*
Sin[f*0.002*n],{n,0,M}],Flatten[Transpose[J][[2]]]],2]]
```

9. References

[1] D. S. Jeong, H. Schroeder, and R. Waser "Mechanism of bipolar switching in a $Pt/TiO_2/Pt$ resistive switching cell," Physical review B 79: 195317, 2009.

[2] D. S. Jeong, H. Schroeder, and R. Waser, "Electrochem, Solid state Lett.," 20 G51, 2007.

[3] M. Rozenberg "Resistive Switching," Scholarpedia 6(4):11414, 2011.

[4] Modelling and Simulation in Materials Science and Engineering 11: R33-R68, 2003.

[5] Olof Runborg "Finite volume discretization of heat equation" Numerical Solutions of differential equations DN2255, 2012.

[6] "Explicit and implicit methods," In *Wikipedia*. Retrieved March 4, 2014 from http://en.wikipedia.org/wiki/Explicit and implicit methods.

[7] "Fermi level," In *Wikipedia*. Retrieved March 26, 2014 from http://en.wikipedia.org/wiki/Fermi level.

[8] D. B. Strukov, G.S. Snider, D. R. Stewart & R. S. Williams "The missing memristor found," Nature 1.1038/ 06932, 2008.

[9] "Memristor," In *Wikipedia*. Retrieved December 4, 2013 from http://en.wikipedia.org/wiki/Memristor.

[10] P. Frey M.d. Buhan "The finite difference method" ma691: R 79 - R 92, 2008

[11] E. G. Karpov "Bistability, autowaves and dissipative structures in semiconductor fibers with anomalous resistivity properties," Philosophical Magazine Vol. 92, No. 10, 1300–1316, 2012.

[12] A. Maria "Introduction to modeling and simulation" Proceedings of the Winter Simulation Conference, 1997.

[13] M. Barbarossa “Basics of Mathematical Modeling” Lecture Notes of Prof. C. Kuttler, 2010.

[14] D. Slavsky “Introduction to discretization,” phys301: 2009.

[15] “Mathematica,” In *Wikipedia*. Retrieved October 10, 2013 from http://en.wikipedia.org/wiki/Mathematica.

[16] S. M. Sze, K. K. Ng “Physics of Semiconductor Devices,” New York: Wiley, 3rd ed., ISBN 0-471-14323-5, 2006.

[17] “Euler Method,” In *Wikipedia*. Retrieved October 10, 2013 from http://en.wikipedia.org/wiki/Euler_method.

MANASI HEMANT KULKARNI

2306 W Taylor St. Apt 2 Chicago, IL 60612 | 312-515-4504 |mkulka4@uic.edu

University of Illinois at Chicago | Chicago, IL 60608

EDUCATION

August 2014 | M.S. Material Engineering

University of Illinois at Chicago, Chicago, IL

May 2012 | B.Tech Metallurgy and Materials Engineering

Visvesvaraya National Institute of Technology, Nagpur, India

RESEARCH EXPERIENCE

May 2012 | Bachelor's student, Visvesvaraya National Institute of Technology, Nagpur, India

Bachelor's Thesis: Porous High entropy alloys

- Consolidation of porous high entropy alloy AlFeCrNiMn,
- Three pellets consolidated by cold compaction and sintering.
- Morphology, densification and electrochemical properties were studied.
- X ray diffraction, Differential thermal analysis, cold compaction, Scanning electron microscope, Potentiostat were used to perform respective experiments.

July 2011 | Research Intern, Indian Institute of Technology, Bombay, Powai, India

High strength High conductivity copper

- Electroplating of Copper using both direct plating and pulse plating techniques
- The effect of deposition parameters on the quality of film and on its adhesion to the substrate was studied.
- In all 14 different deposition conditions were tried and a set of conditions for obtaining good quality coatings was evolved.
- The morphology of film was studied using Optical Microscopy and Scanning Electron Microscopy.

June 2010 | Summer Intern, TATA MOTORS, Pune, India

Hexavalent and Trivalent Chromium Passivation comparison

- Commercial processes of plating and passivation were studied while comparing advantages and disadvantages of both passivation processes.
- Corrosion resistance of nine different automotive parts was tested by salt spray test to conclude that trivalent chromium will achieve better properties by development in passivation techniques.
- A graph depicting corrosion resistance vs. plating thickness was also plotted. Material analysis was done by X-ray diffraction.